Nanoscale Characterization of Aged Li-Ion Battery Cathodes

THESIS

Presented in Partial Fulfillment of the Requirements for the Degree Master of Science in the Graduate School of The Ohio State University

By

Sanjay Ramdon, B.S.

Graduate Program in Mechanical Engineering

The Ohio State University

2013

Master's Examination Committee:

Professor Bharat Bhushan, Advisor

Professor Lei (Raymond) Cao

Abstract

Lithium-ion (Li-ion) batteries have become very prominent as a form of energy storage for numerous applications due to its high energy and power densities. They are used for numerous portable devices and more recent electric vehicles (EVs). It is important to increase the cycle life of Li-ion batteries in order for them to be more viable for the automotive industry. With use, these batteries undergo an aging process which reduces the battery storage capacity and increases internal resistance. To reduce the aging process it is essential to first understand the degradation mechanisms on the electrodes of the battery.

A multi-scaled approach has been previously applied to the study of the degradation of the $LiFePO_4$ cathodes. It has been shown that nanoparticles in cathodes coarsen as a result of aging. Coarsening of nanoparticles has been shown to lead to an increase in surface resistance and decrease in surface conductivity, which is responsible for reduced lithium retaining capacity. It is therefore important to study the cause of these aging mechanisms in order to increase the life of the battery. An in depth study of cathode on the nanometer scale is necessary using atomic force microscope (AFM) related techniques.

In this work, both ex-situ and in-situ studies were conducted to understand the aging phenomenon in $LiFePO_4$ battery cathodes. High resolution AFM imaging and current measurements were conducted to study the difference of the unaged cathode from the aged. This was done to quantify the coarsening process. Particle agglomeration was observed in the aged cathode, which is believed to reduce surface conductivity.

Nanomechanical characterization and mechanical integrity studies were then conducted on unaged and aged cathodes using AFM equipped with nanoindentor. This was done to determine the effect of increased internal stress within the cathode created during aging on the nanomechanical and mechanical integrity properties. Properties of hardness, elastic modulus, creep, nanowear, nanoscratch and nanofriction were examined and significant differences were observed between unaged and aged cathodes. The aged cathodes showed higher hardness, creep depth and critical load in scratch and lower wear depth and coefficient of friction.

In order to further understand aging mechanisms, real time examination of battery cathodes were done during operation of the cell using in-situ techniques. AFM in-situ techniques allow direct observation of cathodes during cycling of the cell on the nanometer scale. Morphology data showed increase in particle size from $FePO_4$ phase to $LiFePO_4$ phase during discharge of the cell due to lithiation. In-situ AFM electrochemical characterization has been shown to be a useful technique to study Li-ion battery aging mechanisms.

These studies further the understanding of the degradation mechanisms of Li-ion battery cathodes. The in situ electrochemistry approach advanced in this work is believed to be useful for fundamental understanding of aging mechanisms.

Dedication

This thesis is dedicated to my family and friends.

Acknowledgments

First and foremost I would like to thank my advisor Professor Bharat Bhushan for giving me the opportunity to work in his research laboratory. Working in this lab has been a wonderful experience for me both personally and professionally. Professor Bhushan has inspired me to perform my work at the highest level with integrity and discipline.

I would like to personally thank all of my colleagues at the NLBB who I have had the privilege of working with for their technical discussions and friendship, especially Dave Maharaj and Greg Bixler. I would also like to thank Dr. Shrikant Nagpure who provided guidance and assistance to the success of my research. Sincere thanks to Dr. D. Emre Demirocak and Dr. Adythia Kumar for providing technical discussion and experimental guidance towards the completion of this work. Thanks to Dr. Song Xu for providing instrumentation support. I am also grateful to Dr. Hyungoo Lee and Dr. Manuel Palacio whose technical discussions and scientific advice has aided me in my endeavors. A special thanks to Jeneen Sands and Nicklaus Breckenridge for their encouragement and guidance throughout my program duration.

Most importantly, I would like to thank my family and friends whose unending support and motivation helped push me through to completion of my degree. The loyalty, support, and kind motivation of my friends, has helped drive me to new heights

and pull me through hard times. Special thanks to Lara Jane Hadlocon for invaluable support. Lastly, my parents, Rosalee and Raymond Ramdon, whose work ethic, morals, and love have been unwavering, and my siblings Sheneka and Roopchan, who have provided guidance and the motivation I needed.

Vita

November 8, 1988 .....Born – Jamaica

2007-2011.....B.S. Engineering Mathematics, Saint Augustine's University, Raleigh, NC

2011-Present .....Graduate Research Fellow, Department of Mechanical Engineering, The Ohio State University, Columbus, OH

Publications

1. Ramdon, S. and Bhushan, B. (2012), "High resolution morphology and electrical characterization of aged Li-ion," *J. Colloid and Interface Sci.,* **380**, 187-191.
2. Ramdon, S. and Bhushan, B. (2013), "Nanomechanical characterization and mechanical integrity of unaged and aged Li-ion battery cathodes," *J. Power Sources,* **246**, 219-222.

Fields of Study

Major Field: Mechanical Engineering

Table of Contents

Abstract ii

Dedication v

Acknowledgments vi

Vita viii

Table of Contents ix

List of Tables xii

List of Figures xiii

Chapter 1: Introduction 1

Chapter 2: High Resolution Morphology and Electrical Characterization of Aged Li-ion Battery Cathode 4

2.1 Introduction 4

2.2. Experimental details 6

2.2.1 Li-ion battery samples 6

2.2.2 Morphology 7

2.2.3 Conductivity measurement 8

2.3 Results and Discussion 10

2.3.1 Morphology of $LiFePO_4$ battery cathode 10

2.3.2 Surface conductance of aged and unaged cathodes 15

2.4 Summary and Outlook 18

CHAPTER 3: Nanomechanical Characterization and Mechanical Integrity of Unaged and Aged Li-ion Battery Cathodes 20

3.1 Introduction 20

3.2. Experimental details 24

3.2.2 Nanomechanical characterization 25

3.2.3 Mechanical integrity studies 28

3.3. Results and Discussion 30

3.3.1 Nanomechanical characterization 30

3.3.2 Nanowear experiments 32

3.3.3 Nanoscratch experiments 34

3.3.4 Nanofriction experiments 37

3.4 Summary and Outlook 39

Chapter 4: In situ AFM electrochemical characterization of Li-ion battery cathodes 40

4.1 Introduction 40

4.2 Review of In situ electrochemical cells 42

4.2.1 Optical 43

4.2.2 Electron 44

4.2.3 AFM 49

4.2.3 Neutron techniques 50

4.2.4 X-ray techniques 51

4.2.5 Selection of the technique used in the present study 52

4.3 Experimental details 54

4.3.1 AFM, glove box and potentiostat 54

4.3.2 In situ cell design 58

4.3.3 Extraction of samples from a commercial cell 62

4.3.4 A Commercial Cell for comparison 62

4.3.5 In situ AFM experiment 63

4.4 Results and Discussion 65

4.4.1 Charge/discharge curves of the commercial cell and the Li- wire cell 65

4.4.2. AFM Images of the bare cathode and the cathode in the electrolyte 68

4.4.3 In situ AFM images of cathode during charge and discharge 70

4.5 Summary and Outlook 72

Chapter 5: Summary 74

References 77

List of Tables

Table		Page
3.1	Nanomechanical and friction properties of unaged and aged cathodes	31
4.1	In-situ electrochemical cell for studying Li-ion batteries ……	53

List of Figures

Figure Page

2.1 Surface height and conductivity maps silica (left) and a gold film evaporated on a silicon substrate (right)……..... … 9

2.2 Surface height images of the unaged and aged $LiFePO_4$ cathode samples at various scan sizes……. 11

2.3 Particle size distribution of unaged and aged $LiFePO_4$ cathode images at various scan size……... 13

2.4 RMS roughness as a function of scan size of unaged and aged $LiFePO_4$ cathodes…… 14

2.5 A 5 μm x 5 μm (left) and 2 μm x 2 μm (right) comparisons of both unaged and aged $LiFePO_4$ cathodes. (a) Surface height and conductivity maps for unaged and aged. Arrows indicate line where sections were taken. (b) Profile of surface height and current overlay of both unaged and aged. (c) Histogram of the distribution of the current in the conductivity maps of both unaged and aged…….. 16

3.1 AFM Surface height images with RMS and P-V distance values and

particle distributions of unaged and aged LiFePO4 cathode samples. (Adopted from Ramdon and Bhushan,2012)……..... 22

3. 2 Indentation depth as a function of time for hardness and elastic modulus experiment and load as a function of indentation depth for unaged and aged cathode samples…….. 26

3.3 Load as a function of time for indentation creep experiment and indentation depth as a function of time for unaged and aged cathode samples…….……. 28

3.4 Surface height maps and sections of unaged and aged cathodes showing worn region at 50 μN and 100 μN loads. Average wear depth ($\bar{d}$) are listed in the sections…… 33

3.5 Friction force as a function of load for unaged and aged cathodes and silicon (100) for reference. Coefficient of friction values obtained from the slope of the curves are also presented……. 36

3.6 Coefficient of friction as a function of normal load and height images of unaged and aged cathodes and silicon (100) sample for reference. Arrow in height images of scratched surfaces indicate damaged regions……..... 37

3.7 Bar chart showing hardness (H), elastic modulus (E), average creep depth, average wear depth at 50 μN and 100 μN loads, critical load in scratch and coefficient of friction of unaged and aged cathodes……..... 38

4.1 Schematics of In situ electrochemical cells for (a) Raman, optical and transmission electron microscope (TEM) and scanning electron microscope (SEM), (b) AFM, and (c) for neutron and X-ray experimental techniques. WE, CE and RE represent working electrode, counter electrode and reference electrode respectively…… 46

4. 2 Schematics of (a) AFM and (b) glove box designed for storage as well as electrochemical experiments……..……. 56

4.3 AFM electrochemical cell designs proposed for in-situ electrochemical experiments, (a) three-electrode with cell schematic (top) and commercial cell (bottom), and (b) two-electrode cell design with cell schematic (top), Li-wire cell (middle) and coin cell (bottom). ……... 61

4.4 Charge and discharge curve of a commercial LiFePO4 cell……. 66

4.5 Charge and discharge curve of an experimental wire LiFePO4 cell…… 67

4.6 AFM height and deflection image of bare and in electrolyte LiFePO4 cathode…….. 69

4.7 AFM height and deflection image as well as particle area analysis of LiFePO4 cathode showing change of particle size between charged and discharged states. ……. 71

Chapter 1: Introduction

Development of Li-ion batteries has been driven by an ever-increasing demand for portable electronic devices (Tarascon and Armond, 2001). Since the early 2000s, Li-ion batteries have emerged as energy storage media for electric vehicles (EVs), hybrid-EVs (HEVs) and plug in-EVs (PHEVs) to reduce dependence on non-renewable energy sources. Developing cheap and sustainable energy storage devices will allow EVs to be utilized more as they become more cost effective (Armand and Tarascon, 2008). Li-ion batteries are used in the automotive industry because of their extended cycle life and high energy density per unit weight (specific energy) (Nagpure and Bhushan, 2009; Nagpure, 2011).

According to Tarascon and Armand (2001), a battery is composed of several electrochemical cells connected in series and parallel to provide the required voltage and capacity, respectively. The cell consists of positive and negative electrodes, separator and electrolyte solution containing dissociated salts, which allows ion transfer between the electrodes while inhibiting the electronic conductivity.

Padhi et al., (1997) introduced lithium iron phosphate ($LiFePO_4$) as Li-ion battery chemistry for cathode material. $LiFePO_4$ cathodes have been studied by researchers because of their high theoretical specific capacity ($\approx$170 mAh g^{-1}), high thermal stability,

specific energy (≈ 0.60 Wh g^{-1}), and low toxicity (Borong et al., 2011; Choi et al., 2012; Zaghib et al. 2013).

$LiFePO_4$ is a viable option for meeting the requirements set by the United States Advance Battery Consortium (USABC) for EVs (Anonymous, 2002, 2006a, 2006b). With use, however, the electrochemical properties of Li-ion batteries degrade, which leads to a reduction in the storage capacity. Therefore, it is important to understand the underlying mechanisms of aging phenomenon in Li-ion batteries in order to extend their life (Nagpure, 2011; Nagpure et al. 2013).

Studies were conducted comparing the unaged and aged cathode materials to show their morphological, electrical and structural changes over cycling. The studies on $LiFePO_4$ battery cathodes showed agglomeration of $LiFePO_4$ nanoparticles with aging. The agglomerated particles are believed to consist of smaller particles. Particle sizes for unaged cathodes were between 150 and 250 nm, while larger agglomerated particles for the aged cathodes were between 350 to 400 nm and consisted of smaller particles ranging from 100 to 150 nm. Agglomeration is believed to result in an increase in surface resistance, and decrease in surface conductivity, consequently reducing the battery capacity (Nagpure et al., 2009, Nagpure, 2011; Ramdon and Bhushan, 2012).

Nanomechanical characterization experiments have been conducted to observe the effect of increased internal stress during aging (Ramdon and Bhushan, 2013). Increase in creep and hardness were found to be associated with polyvinylidene difluoride (PVDF) binder degradation and dislocation formation due to the high internal stress and strain created during lithiation and delithiation.

It is vital to conduct in situ AFM experiments to observe real time changes in cathodes. A review of various in situ electrochemical cells for Li-ion battery investigation is presented. Reasons for selecting AFM techniques are given. Different electrochemical cell designs used for in-situ AFM experiments are described. Next, a two-electrode electrochemical cell design is proposed; results of the in situ AFM electrochemical studies on $LiFePO_4$ battery cathodes are presented.

It is important to extend the current life of Li-ion batteries which requires understanding the mechanisms that cause a battery to loose storage capacity with age. Further work on the development of in situ AFM techniques for studying degradation mechanisms is needed to overcome the issues relating to that technique. One of such issue is the evaporation of electrolyte within the cell over time.

Chapter 2: High Resolution Morphology and Electrical Characterization of Aged Li-ion Battery Cathode

2.1 Introduction

In recent years, energy has become one of the most crucial problems in our society, where our current standard of living depends on us being able to cope with its ever increasing demand. Since the first use of the word *battery* by Benjamin Franklin in 1749 to the first rechargeable lead acid cell and now to the present Li-ion batteries, the need for creating portable energy sources has been the fuel for developing better batteries. Batteries are now needed in the automotive industry to reduce our consumption of oil as well as to make more environmentally friendly vehicles (Yang et al., 2011; Tarascon and Armand, 2001).

The Li-ion batteries, first commercialized by Sony Corporation in 1991, has mostly been examined for the purpose of electric vehicles (EV) and has been selected as one of the most viable battery technologies due to its high gravimetric energy density and high specific capacity (Armand and Tarascon, 2008). There are different chemistries for Li-ion batteries such as cobalt oxide, manganese, nickel-cobalt manganese (NCM), and phosphate systems, each of which provides their own advantages and disadvantages. Lithium Iron Phosphate ($LiFePO_4$) was found to be an excellent material for the cathode

of the Li-ion battery when introduced (Pahdi et al., 1997). The $LiFePO_4$ battery has the highest gravimetric energy density (Wh/kg), high theoretical capacity, and high operating voltage of 3.5 V. The battery is low in cost and is environmental friendly (Chung et al., 2002), which makes it preferred over other chemistries.

Aging is an issue with $LiFePO_4$ batteries as the capacity and power of these batteries decrease with multiple charge and discharge cycles (Nagpure, 2011). With these Li-ion batteries being expected to last the life of an electric or hybrid electric vehicle, it is important to understand the specific aging mechanism that is taking place in this Li-ion chemistry as the degradation mechanisms vary with the cathode material used. A multi-scaled approach has been applied to the study of the degradation of the $LiFePO_4$ cathodes (Nagpure, 2011) . Thermal diffusivity was carried out using a flash method to identify regions of damage on the battery cathode on the millimeter scale length (Nagpure et al., 2010), while Kelvin probe and Scanning Spreading Resistance (SSRM) have been used to further characterize the aging that is taking place on the micron scale length (Nagpure et al., 2009, 2011). An in depth study of cathode on the nanometer scale is necessary using high resolution AFM.

In this chapter, high resolution imaging of $LiFePO_4$ cathode is conducted on unaged and aged cells using an AFM (Ramdon and Bhushan, 2012). This provides necessary details of the morphological changes that are occurring at the nanometer scale. Particle size analysis and RMS roughness measurements were used to further study the data collected from the cathodes. In addition, conductance measurement on a small scale

was done to describe the electrical conductance of the sample and to study details within the sample to identify aged locations of the cathode (Nagpure et al., 2010).

2.2. Experimental details

2.2.1 Li-ion battery samples

The cylindrical Li-ion cells used in this experiment have the standard graphite on copper substrate for the anode, while the cathode is made up of $LiFePO_4$ nanoparticles on an aluminum substrate bonded with a polyvinylidene fluoride (PVDF) binder. With a separator in between the anode and cathode they are rolled in a tube, along with lithium hexafluorophosphate ($LiPF_6$) salt in alkaline carbonate which is the electrolyte used to create the cell. The cell has an operating voltage of 3.3 V and a nominal discharge capacity of 2.3 Ah. There is a coating of carbon present on the $LiFePO_4$ nanoparticles to improve conductivity (Goodenough, 2007).

Two commercial lithium ion cells were selected, one of which was unaged. The other, termed the aged, was cycled until it reached its end of life (EOL), at a C-rate of 6C, 60-70% State of Charge (SoC) and at 45ºC. The C-rate is a unit that is used to measure the charging and discharging currents of a battery. A charge rate of 1C for a battery of 2.3 Ah will take 1 h to charge and similarly, if discharged at 1C it would take a hour to discharge at 2.3 A. For 6C, it would take 1/6 h to charge and 1/6 h to discharge if it is discharged at a current at 6(2.3)= 13.8 A. SoC represents the level at which the battery

is charged before it is then discharged to complete a cycle. The EOL occurs when the cells storage capacity drops by 20% (Nagpure et al., 2009). The cells were then discharged completely and disassembled in air and the long strips of cathode were extracted. The samples for this study were then cut from an area close to the center of the cell for the unaged and aged, the center was chosen because it was shown by thermal diffusivity to have greater signs of aging.

2.2.2 Morphology

The AFM used in this experiment was the Agilent 5500 AFM (Agilent Technologies Chandler, AZ), used in the Acoustic AC Mode (this mode is similar to "tapping mode" in other AFMs) to obtain the high resolution images of the $LiFePO_4$ cathode. This mode involves using a piezo-electric transducer in the AFM to oscillate the cantilever at its resonant frequency. When the tip is brought close to the sample contact occurs when the oscillation of the cantilever is dampened by the surface at a set percentage. As the tip is scanned across the surface to make one scan line the AFM will adjust its piezo voltage on the Z axis to maintain the specified amplitude set point. The AFM uses the correction signal as a source to plot the topography of the surface. The probe used in this study was a silicon cantilever with a tip radius of less than 10 nm, nominal force constant of 48 N/m and resonance frequency at a nominal value of 190 KHz (Nanosensors PPP-NCL). A scan rate of 1 Hz was used.

Particle size analysis was then carried out using the image processing software Image Metrology SPIP (Denmark). Surface roughness analysis was done by taking roughness measurements of multiple images at each scan size interval and then taking an average. Six measurements at minimum were taken at each scan size of the unaged and aged samples.

2.2.3 Conductivity measurement

Current sensing atomic force microscopy (CSAFM) was used to image the surface of the $LiFePO_4$ cathode using an Agilent 5500 AFM equipped with a current sensing preamplifier. The amplifier had a sensitivity of 1 nA/V. CSAFM experiments were conducted in contact mode where the tip is traced across the surface. A tip that was coated with conductive material was used. CSAFM involves a bias voltage applied between the sample and the tip which creates a current and this current is used to construct a conductivity map. The voltage used in this experiment was 3 V. A calibration of the preamplifier was done before starting each experiment and the curve was as expected for the preamplifier in each instance. This proves that the device was accurately calibrated. Agilent Pico Image was used to conduct the data analysis. The probe used was a silicon probe coated with platinum (Micro Mash CSC11/Pt) to allow conductivity and had a force constant of 0.35 N/m. A scan speed of 0.5 Hz was used.

A demonstration sample was prepared to show that the CSAFM module was working as it was designed. One sample was prepared from a single crystal silicon (100)

wafer. Another sample was prepared by depositing gold of 100 nm thickness onto silicon a wafer by thermal evaporation. CSAFM data was collected of each sample and is shown in **Fig. 2.1.** It shows the AFM surface height image on the top for both silicon and a gold plated silicon substrate. The conductivity map shown in **Fig. 2.1** compares the silicon wafer with the silicon wafer plated with gold. The gold plated wafer displays significantly higher currents than the unplated wafer. The current readings were extremely low for the silicon while the values for the gold plated silicon were higher ranging from 0 to 10 nA. This test confirmed that the AFM equipped with a CSAFM (Current Sensing AFM) was in good working order and that the data that was obtained is accurate.

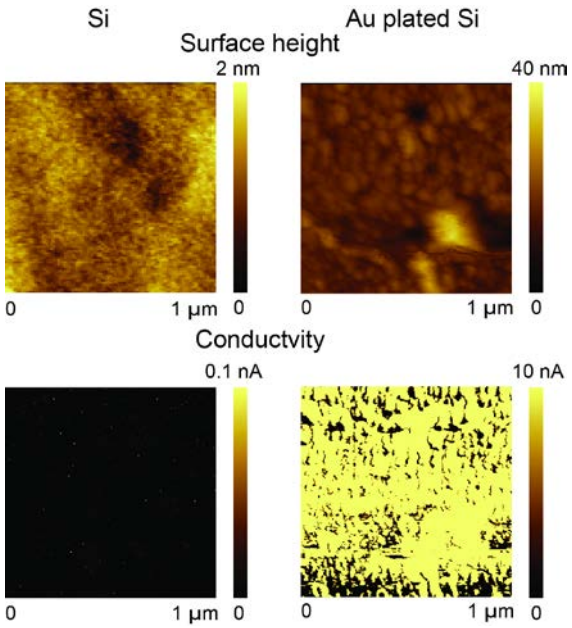

Fig. 2.1. Surface height and conductivity maps silica (left) and a gold film evaporated on a silicon substrate (right).

2.3 Results and Discussion

2.3.1 Morphology of $LiFePO_4$ battery cathode

The high resolution surface height image of the $LiFePO_4$ cathodes in **Fig. 2.2** shows three scan sizes decreasing from 5 μm x 5 μm to 0.5 μm x 0.5 μm, showing the agglomeration of the particles as a result of coarsening on the cathode. On the unaged 5 μm x 5 μm cathode, rather uniformly shaped particles can be seen, as opposed to the aged where there is evidence of large particles composed with smaller particles. When examined at a small scan size of 0.5 μm x 0.5 μm one clearly sees evidence that these larger particles are composed of multiple smaller particles.

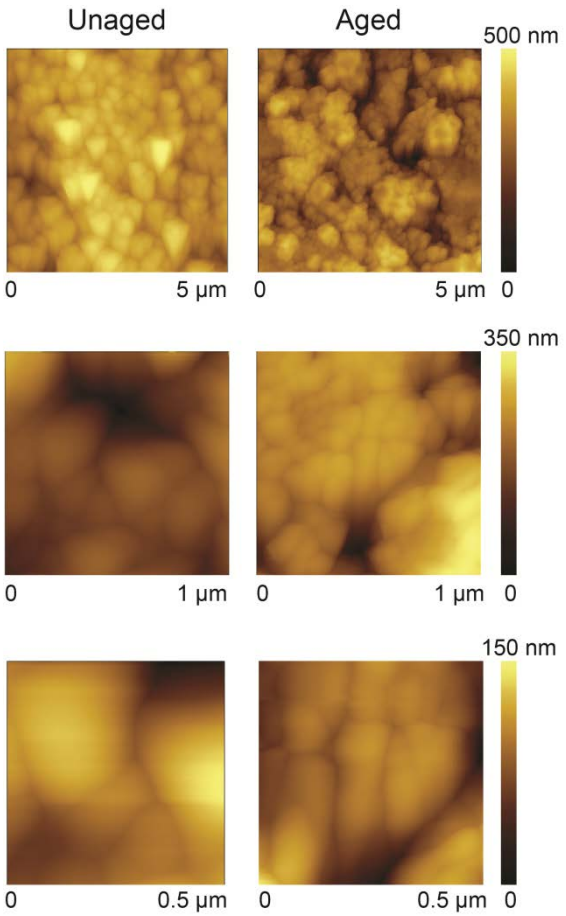

Fig. 2.2. Surface height images of the unaged and aged LiFePO4 cathode samples at various scan sizes.

The small particles may have formed as a result of phase transformation of the $LiFePO_4$ particles that occurs during intercalation and deintercalation of Li^+ from the cathode during cycling. They may be nanocrystalline deposits (NCD) on the surface of the cathode. NCD were proposed to be occurring on $LiFePO_4$ by Nagpure et al. (2009), but further evidence was needed to confirm. They have been observed on the $LiNi_{0.8}Co_{0.2}O_2$ by Zang et al. (2001) and Kostecki and McLarnon (2002), where they

were proposed to form from the cobalt and nickel oxide phase segregation through the Ni^{3+} and Co^{3+} solid-state diffusion

Another factor that may account for the drastic surface change of the cathode is the mechanical stress created as the Li^{+} ion intercalates and deintercalates into the surface of the cathode which leads to large particles breaking up into smaller particles. This was proposed by Zang et al. (2001) as a possible explanation of the degradation found in $LiNi_{0.8}Co_{0.2}O_2$, where the mechanical stress is caused by the nonhomogeneous lithium distribution within large agglomerates. Kerlau et al. (2007) suggested that the active material of $LiNi_{0.8}Co_{0.2}Al_{0.05}O_2$ and $LiNi_{1/3}Co_{1/3}Mn_{1/3}O_2$ deteriorate during cycling/aging due to repeated mechanical stress. Balke et al. (2010) reported a change in volume and strain produced within $LiCoO_2$ cathode material during intercalation and deintercalation of lithium.

For $LiCoO_2$ cathode Balke et al. (2010) reported that the orientation of the grain would influence the performance of the cathode. Based on high-frequency bias experiments, the lithium ions were found to easily diffuse along the lithium layer which is parallel to the (001) plane of the hexagonal unit cell and not perpendicular to the lithium layer in the [001] direction due to the closed pack oxygen layer. Chen et al. (2006) reported that movement of Li ions to be anisotropic in $LiFePO_4$. In the delithiated form $FePO_4$, Li ions were confined to move back along the *b*-axis (space group *Pnma*). The morphological changes within the cathode observed in **Fig. 2.2** may lead to re-orientation of active material in the cathode which may lead to reduced Li-ion diffusion.

Particle size analysis was carried out on at least five images at different scan sizes to determine the size distribution. **Fig. 2.3** shows that most of the particles for the unaged are between size 150 to 250 nm. This was compared to the aged cathode which had most of the particles ranging between 100 to 150 nm. Thus the particles of the aged cathodes are on average smaller than the unaged. With high resolution AFM imaging smaller particles can now be differentiated, whereas before they might have been interpreted as one large uniform particle.

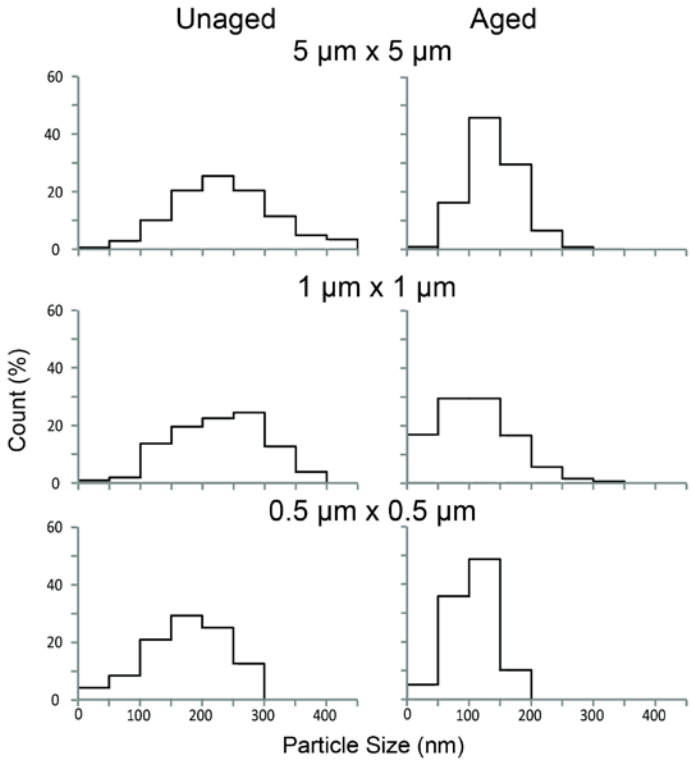

Fig. 2.3. Particle size distribution of unaged and aged LiFePO4 cathode images at various scan size.

The roughness analysis shown in **Fig. 2.4** was carried out on various scan sizes ranging from 10 μm x 10 μm to 0.3 μm x 0.3 μm. Each data point represents an average of at least six roughness measurements which were calculated from different images at the same scan size. The aged sample is rougher at each scan size as compared to the unaged sample which may suggest that the aged surface comprises of smaller particles. Increasing roughness values with an increase in the sample size has to do with the sampling length (Thomas, 1999; Bhushan, 2002).

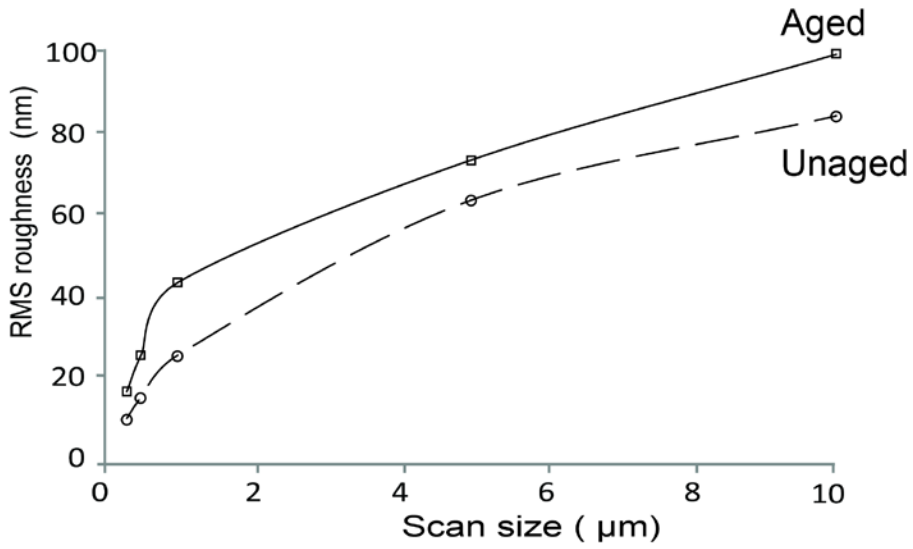

Fig. 2.4. RMS roughness as a function of scan size of unaged and aged LiFePO4 cathodes.

2.3.2 Surface conductance of aged and unaged cathodes

The current sensing AFM was used to obtain the data shown in **Fig. 2.5**. Analysis was carried out on both the unaged and aged at 5 μm x 5 μm and 2 μm x 2 μm. The data shows significantly lower currents recorded in the aged cathode than in the unaged cathode. In **Fig. 2.5(a)**, the scale chosen for the conductivity map is set to 0.01 nA and all the areas within the sample that are white means that area can have higher current reading that 0.01 nA. This was done to accurately show details within the sample and allows the determination of particle boundaries in the current map. High current values mean the area is conductive. There is a greater occurrence of higher conducting regions within the sample for both 5 μm x 5 μm and 2 μm x 2 μm for the unaged cathodes. In the aged sample it is observed that the particles and agglomerated regions show little conductivity and only the edges of some particles show conductivity.

Fig. 2.5(b) shows a profile extraction that was done for the unaged and the aged, and it is seen that there are higher currents in the unaged going up to 2 nA for that section as compared to the aged with the highest reading being 0.01 nA. The 2 μm profile of the unaged sample shows that the particles have higher current reading as compared to the aged samples that have very low conductance. **Fig. 2.5(c)** shows the histogram of all the current data extracted from the current map. The unaged shows readings that are significantly higher than the aged. The unaged sample shows that 20% of the values fall between 1 to 10 nA while the other 80% are distributed from 0 to 1 nA. The majority of the aged cathode current values fall between 0 and 0.1 nA.

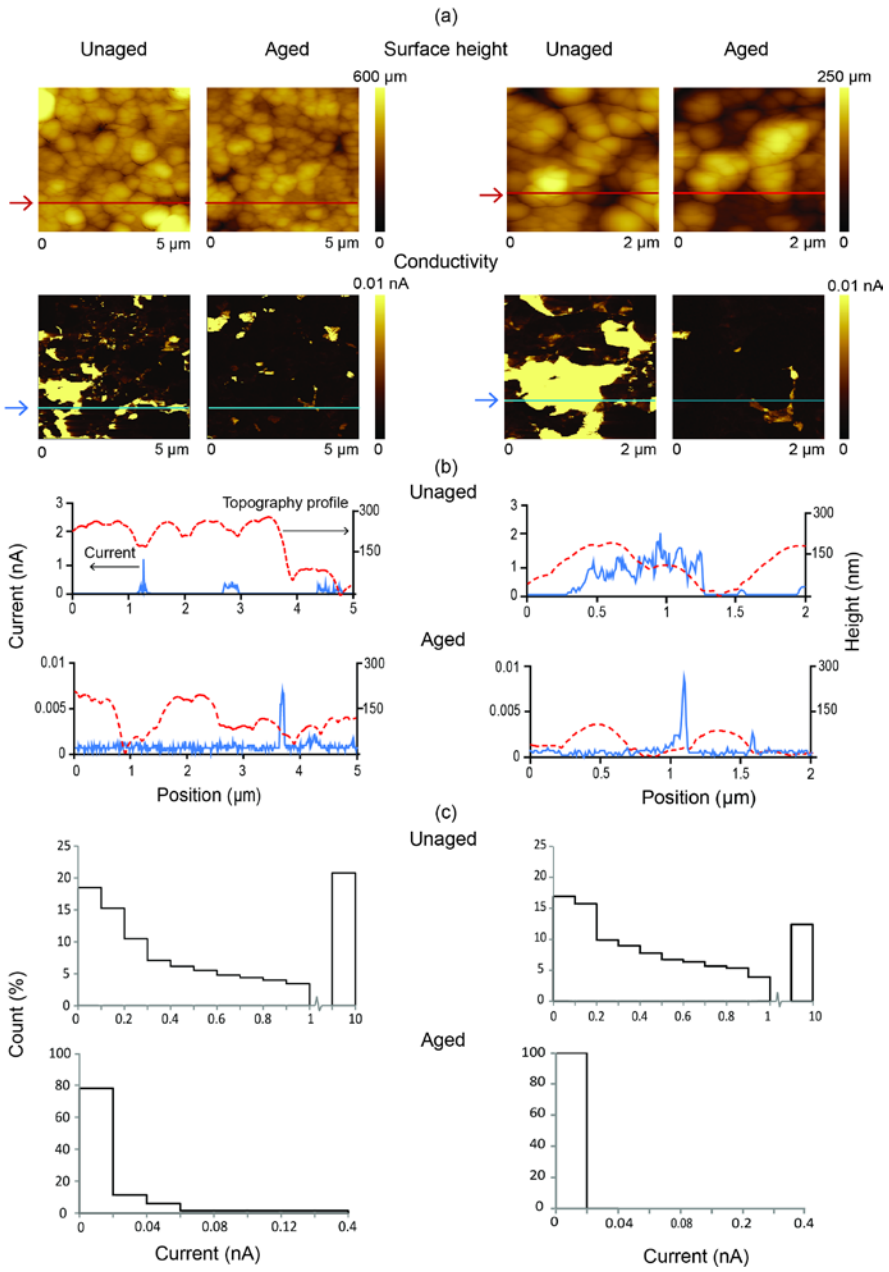

Fig. 2.5. A 5 µm x 5 µm (left) and 2 µm x 2 µm (right) comparisons of both unaged and aged LiFePO4 cathodes. (a) Surface height and conductivity maps for unaged and aged. Arrows indicate line where sections were taken. (b) Profile of surface height and current overlay of both unaged and aged. (c) Histogram of the distribution of the current in the conductivity maps of both unaged and aged.

Conduction is important within the Li-ion cell as there are multiple interphases and the need for electrical conduction to be present for the cell to perform as designed (Park et al., 2010). The surface conductivity is important as it influence the rate at which the Li-ions are being diffused from the cathode to the anode during charging and would thus cause an ionic resistance if reduced.

There are a number of possible explanations for the occurrence of the extremely lower conduction of the aged cathode. There can be a loss in contact of the $LiFePO_4$ particles from the conductive backbone of the cathode or there can be a layer on the surface which insulates the particles from the probe. Conductive studies were carried out on $LiNi_{0.8}Co_{0.2}Al_{0.05}O_2$ and $LiNi_{1/3}Co_{1/3}Mn_{1/3}O_2$ the aged cathodes at a 5 μm x 5 μm scan size showed significantly lower conductivity (Kerlau et al., 2007; Shim et al., 2002). This was attributed to the active material losing contact with the substrate, poor conductivity of the PVDF binder, and the rearrangement of the carbon additive. Carbon is added to the cathode as an additive to increase the conductance of $LiFePO_4$ particles (Goodenough, 2007). This carbon might be degraded or rearranged due to morphological changes that are occurring on the surface of the cathode. This would be an explanation for observing conductance along the edges of particles in **Fig. 2.5(a)** where the carbon would be rearranged to the edges of the particles. **Fig. 2.5(c)** shows that the aged cathode is not conductive and has high surface resistance. This may suggest the presence of multiple insulating regions on the surface of the cathode.

Elazari et al. (2010) reported that for lithium-sulfur cells, surface conductivity was reduced with cycling as well as capacity of the cell was reduced; however there was still bulk conductivity within the cathode by cross sectional conductivity analysis. Although there might be conduction in the bulk of the electrode the surface conduction is vital to the performance of the cell as conductance is required for lithium to intercalate and deintercalate.

2.4 Summary and Outlook

High resolution images of aged and unaged $LiFePO_4$ cathodes were obtained at different scan sizes and upon particle size and roughness analysis it was found that the surface of the aged cathodes showed particle agglomeration. The agglomerated particles are believed to consist of small particles produced by the break up and/or formation of nanocrystalline deposits. Particle sizes for unaged cathodes were between 150 and 250 nm, while larger agglomerated particles for the aged were in the range of 350 to 400 nm which consisted of smaller particles of sizes ranging from 100 to 150 nm.

Conductivity measurements show aged sample to have poor electrical conductivity. The carbon coating on the particle needed for the conductivity might be degraded during agglomeration and observed by morphological changes. The loss of contact of the active material from the current collector, possibly loss of carbon and insulating PVDF binder lead to increased resistance in the cathode and hence significantly lower conductivity. These degradation issues which lead to morphology and

conductivity changes will lead to battery capacity reduction and ultimately reduce the life of the battery.

CHAPTER 3: Nanomechanical Characterization and Mechanical Integrity of Unaged and Aged Li-ion Battery Cathodes

3.1 Introduction

Reliance on battery technology has drastically increased as there is a need for portability in performing daily activities. This need for greater portability requires greater storage capacity with compact sizes. A battery is a device that stores chemical energy and converts it to electrical energy when needed. Battery types vary with chemistries and shape, some of which are lead-acid, nickel-cadmium, nickel-metal hydride and lithium ion (Li-ion). Li-ion batteries have been identified to provide high specific energy. Li-ion battery usage rapidly expanded with numerous applications in portable electronics, power tools and transportation. In the transportation industry batteries are needed in order to reduce reliance on oil and to yield more environmentally friendly vehicles (Nagpure and Bhushan, 2009; Nagpure, 2011; Nagpure et al., 2013).

Lithium iron phosphate ($LiFePO_4$), which was first introduced in 1997 (Pahdi et al., 1997), was found to be a good choice for cathode material. The $LiFePO_4$ cathode has been studied extensively because of its high specific capacity (on the order of 170 mAh g^{-1}), high thermal stability, high specific energy (on the order 0.60 Wh g^{-1}) as well as low cost and low toxicity (Borong et al., 2011; Choi et al., 2012; Zaghib et al. 2013). $LiFePO_4$

is considered one of the best options in achieving the United States Advance Battery Consortium (USABC) goals for EVs and PHEVs (Anonymous, 2002, 2006a, 2006b).

During the operation of a Li-ion battery, charge and discharge cycles reduce its capacity and power. It is therefore important to study the cause of these aging mechanisms in order to increase the life of the battery. One such mechanism was found to be coarsening of $LiFePO_4$ particles in aged cathodes by particle agglomeration as shown in **Fig. 3.1** (Nagpure et al., 2009; Ramdon and Bhushan, 2012). The agglomerated particles are believed to consist of small particles produced by the break up and/or formation of nanocrystalline deposits. Particle sizes for unaged cathodes were between 150 and 250 nm, while larger agglomerated particles for the aged were in the range of 350 to 400 nm which consisted of smaller particles of sizes ranging from 100 to 150 nm. Coarsening of nanoparticles has been shown to lead to an increase in surface resistance and decrease in surface conductivity, which is responsible for reduced lithium retaining capacity.

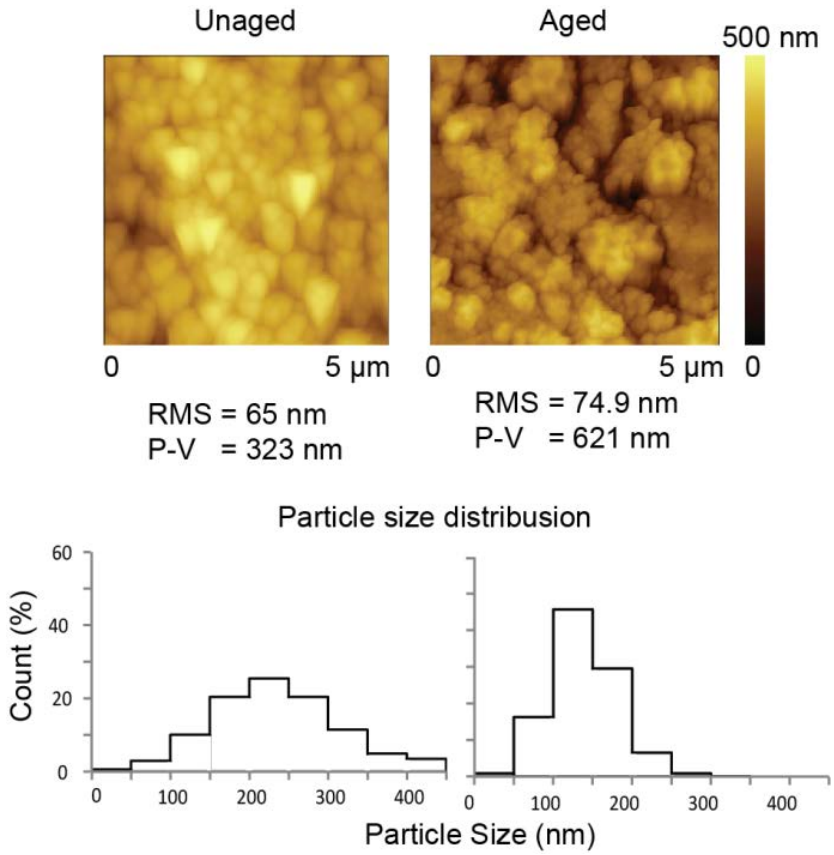

Fig. 3.1. AFM Surface height images with RMS and P-V distance values and particle distributions of unaged and aged LiFePO4 cathode samples. (Adopted from Ramdon and Bhushan, 2012)

Wang (2005) observed crack propagation in $LiFePO_4$ cathode material after cycling using a scanning electron microscope. This was stated as a result of high internal strain during lithiation and delithiation in the cathode particles. A volume change of approximately 7% was observed by Meethon et al. (2007) to occur during lithiation and delithiation while the chemistry of nanoparticles change between $LiFePO_4$ and $FePO_4$ phases.

Simulations of intercalation stresses carried out by Christensen and Newman (2006) and Zhang et al. (2007) on $LiMn_2O_4$ battery electrode particles showed that larger particles produced larger stresses during intercalation. Based on a study of the effect of stress accumulation within the $LiFePO_4$ cathode, Huang and Wang (2012) reported that dislocations and distortion zones were formed through phase transformation of $LiFePO_4$ particle during lithiation and delithiation. It was suggested that this formation and movement of dislocation would lead to crack formation in the cathode. The high internal stresses created during charge and discharge can lead to change in nanomechanical properties and degradation of mechanical integrity of the cathode.

It is of interest to conduct nanomechanical characterization to examine properties such as hardness (H), elastic modulus (E) and creep. Studying hardness is a measure of the cathodes' plastic deformation property while elastic modulus gives the information about elastic deformation. Creep provides information about the viscoelastic nature of the cathode. Mechanical integrity can be studied by performing various durability experiments which include nanowear, nanoscratch and nanofriction experiments (Bhushan, 2011, 2013). The Nanowear experiment can simulate repeated loading and unloading of the cathode. Conducting nanoscratch investigation will allow studying the failure mechanism of the cathode. Scratch resistance can be obtained by observing the changes in friction. It is also important to examine friction on the nanoscale as this can be used as an indicator to the change in the mechanical properties of the cathode (Bhushan 2011, 2013).

In this chapter, nanomechanical characterization and mechanical integrity studies were carried out on unaged and aged $LiFePO_4$ battery cathodes using an AFM and nanoindentor (Ramdon and Bhushan, 2013). To conduct nanomechanical characterization, hardness (H), elastic modulus (E) and creep experiments were performed. For mechanical integrity studies, nanowear, nanoscratch and nanofriction experiments were performed.

3.2. Experimental details

3.2.1 Li-ion battery samples

Cylindrical Li-ion cells used in the experiments have cathode material on an aluminum current collector made of $LiFePO_4$ nanoparticles with polyvinylidene fluoride (PVDF) binder and carbon coating added for increased conduction. Graphite on a copper current collector is used as the anode and lithium hexafluorophosphate ($LiPF_6$) salt in alkaline carbonate solvent as the electrolyte. The anode and cathode are separated by a separator and are rolled in a tube to create the cell. The cell has an operating voltage of 3.3 V and a nominal discharge capacity of 2.3 Ah.

Two identical commercial cells were selected, one termed unaged and the other aged. The unaged cell was charged and discharged completely at 1C (1C = 2.3 Ah) to verify its capacity. The aged cell was cycled until end of life (EOL) was reached. This is defined according to the automobile industry as when the cell's capacity is reduced by

20% (Anonymous, 2006b). The aged cell was cycled at a C-rate of 7C, between 60 and 75% state of charge (SoC) and at 45 °C (Nagpure et al., 2011). The C-rate is a unit that is used to measure the charge and discharge currents of a battery. A charge rate of 7C means it would take 1/7 h to charge and 1/7 h to discharge if it is discharged at a current of 7(2.3) = 16.1 A. SoC range represents the level at which the battery is charged then discharged to complete a cycle. The lifespan of the battery will depend on the rates at which the battery is charged and discharged, the state of charge region and temperature in which the battery was operated. The cells were then discharged completely and disassembled in a glove box filled with Argon atmosphere with dew point of about -34 °C. The $LiFePO_4$ cathode samples used in this study were then taken from the unaged and aged cells and sections close to the center of the cell were chosen because the center was shown by thermal diffusivity to have greater signs of aging (Nagpure et al., 2010).

3.2.2 Nanomechanical characterization

The hardness and elastic modulus of the cathode samples were measured using a probe based scanning nanoindenter head (TS 75 Triboscope, Hysitron, Inc.) which was attached to an AFM (Bruker Dimension 3100, Santa Barbara, CA) with a diamond Bercovich tip (~ 100 nm radius). Nanoindentations were conducted in displacement control mode and a maximum indentation depth of 1000 nm was used for each indent. This depth was chosen to allow sufficient penetration into the cathode to avoid surface roughness effect in the hardness measurement. Nanoindentation depth as a function of

time schematic of the experiment is shown in **Fig. 3.2** (top). The load was ramped until the depth of 1000 nm in 10 s was reached and then the surface was unloaded in 10 s. A minimum of 20 nanoindentations were performed at different locations and the hardness (H) and elastic modulus (E) were calculated using the Oliver and Pharr (1992) method. The average value of hardness and elastic modulus were then calculated along with standard deviation.

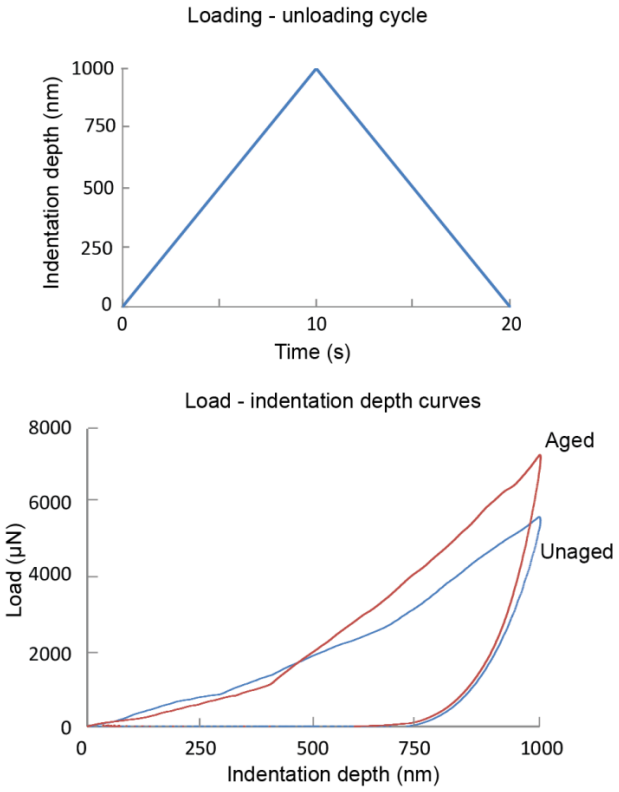

Fig. 3.2. Indentation depth as a function of time for hardness and elastic modulus experiment and load as a function of indentation depth for unaged and aged cathode samples.

Creep tests were performed using load control where a constant load of 1000 μN was applied for 60 s using the nanoindentor with a diamond Bercovich tip (~ 100 nm radius). The load was chosen to provide enough penetration depth into the cathode. A minimum of six creep experiments were carried out on both samples at different locations and the average creep from each sample was calculated. The average creep depth was calculated by averaging the difference in indentation depth at the beginning and end of the constant load applied among the six experiments for each sample. Load as a function of time is shown in **Fig. 3.3** (top).

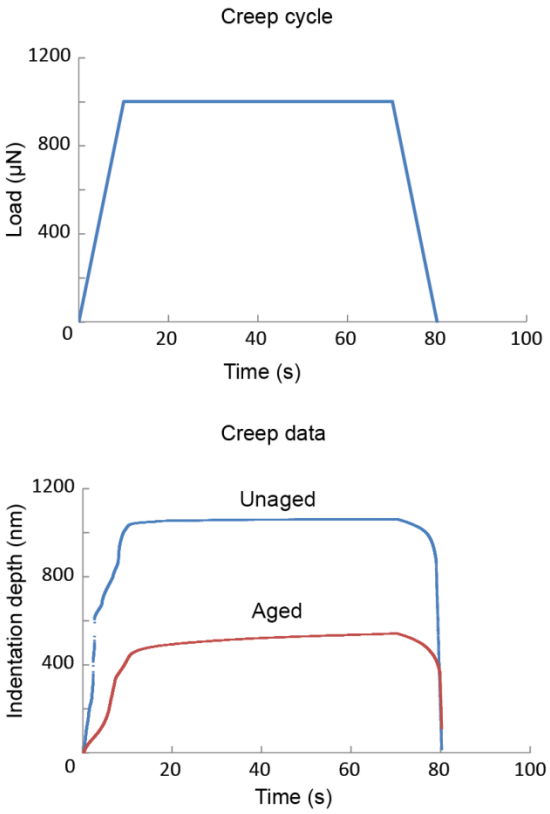

Fig. 3.3. Load as a function of time for indentation creep experiment and indentation depth as a function of time for unaged and aged cathode samples.

3.2.3 Mechanical integrity studies

Nanowear, nanofriction and nanoscratch experiments were performed using the probe based scanning nanoindentor previously described. In nanowear experiment a 5 μm diamond conical tip (60^0 cone angle) was used. During nanowear a scanning speed of 2 μm s^{-1} was used and an area of 5 μm x 5 μm was scanned. Cathode surfaces of 10

μm x 10 μm were scanned before and after the wear experiment at a scanning speed of 0.7 μm s^{-1} such that initial and final surface topography of the wear region as well as surrounding areas were obtained. Loads used were 50 and 100 μN for 1 wear cycle for each sample. Average height decrease of worn area was measured as average wear depth of worn area.

A 20 μm diamond conical tip (90^0 cone angle) was used for the nanoscratch experiment. Scratch was performed with the increase in applied normal load from 0 μN to 350 μN through a scratch length of 10 μm for 10 s. An AFM image of the surface was taken before and after the scratch at a scan speed of 1 Hz. The coefficient of friction at each point was calculated by dividing the friction force by the normal load. The coefficient of friction as a function of normal load was then plotted to determine the critical load of the surface, at which the coefficient of friction increases rapidly (Bhushan, 2013).

Nanofriction experiments were carried out using a 20 μm diamond conical tip (90^0 cone angle). The experiments were performed in the load range of 50 to 300 μN for 10 μm scratch length with a scratch speed of 1 μm s^{-1}. These experiments were performed five times at different surface locations for each load. The average friction force as a function of load was plotted for each sample. The coefficient of friction was obtained as the slope of friction force versus applied normal load curve.

All measurements in this study were obtained under the same ambient atmosphere (22 ± 1 ºC and 45 ± 5% RH).

3.3. Results and Discussion

Nanomechanical characterization and mechanical integrity studies of unaged and aged $LiFePO_4$ battery cathodes were performed, and results of hardness, elastic modulus, creep, nanowear, nanoscratch and nanofriction are presented in this section.

3.3.1 Nanomechanical characterization

Nanomechanical properties of the unaged and aged cathodes were measured using nanoindentation technique. Measured hardness and elastic modulus of the cathode were measured from the load as a function of indentation depth curve as shown in **Fig. 3.2** (bottom). The average hardness and elastic modulus obtained for the unaged and aged cathodes are reported in **Table 3.1**. The unaged cathode has a hardness of 64 MPa and the hardness of the aged was found to be 124 MPa. As discussed in the introduction section, the high internal stress and strain created in $LiFePO_4$ cathode during lithiation and delithiation are believed to form dislocations which may lead to the hardening of the cathode. The elastic modulus of both unaged and aged cathodes is about the same when the measurement error was considered.

Table 3. 1. Nanomechanical and friction properties of unaged and aged cathodes.

Properties	Unaged	Aged
H (MPa)	64 ± 7	124 ± 17
E (GPa)	4 ± 0.5	4.1 ± 0.4
Av. creep depth in 60 s (nm)	14 ± 2	49 ± 3
Wear depth - 50 µN (nm)	478 ± 32	109 ± 19
Wear depth - 100 µN (nm)	906 ± 43	131 ± 21
Critical load in scratch (µN)	120 ± 9	175 ± 12
Coefficient of friction	0.42 ± 0.02	0.30 ± 0.02

In order to understand the creep behavior of the cathode, a 1000 µN load for 60 seconds indentation on unaged and aged cathodes were performed. The resulting indentation depth as a function of time are presented in **Fig. 3.3** (bottom) for unaged and aged cathodes. Indentation depth increases on average 13 nm with the unaged cathode (**Table 3.1**) and the aged cathode increase on average by 49 nm. This data suggested that the aged cathode shows high creep behavior while unaged cathode shows low creep behavior. Hackney et al. (2012) studied creep behavior of Sn-C/PVDF composite anode for Li-ion batteries using the nanoindentation method and reported that creep occurs,

which was used as a measure of failure of the composite structure. For the $LiFePO_4$ cathode, the creep could occur due to the change in the viscoelastic properties of the PVDF binder as the cathode ages. This would suggest evidence of binder degradation occurring in the cathode.

3.3.2 Nanowear experiments

Nanowear experiments were performed on unaged and aged cathodes at 50 and 100 μN loads. The average height decrease of worn area was measured as the average wear depth of worn area. Wear of a 5 μm x 5 μm of unaged and aged cathodes are shown in **Fig. 3.4** for both 50 μN and 100 μN load. It can be observed that the unaged surface showed greater wear of the cathode than the aged. **Table 3.1** shows the average wear depth that was obtained. For 50 μN load the average wear for the aged cathode is 109 nm and for the unaged 476 nm. The degree of wear in the aged cathode is 77.5 % less than that of unaged cathode. At 100 μN load the average wear depth for unaged cathode is 906 nm and for aged is 131 nm, equivalent to 85% reduction in wear for aged cathode. The hardness of the aged cathode is 48% greater than that of the unaged and this is reflected in the nanowear results.

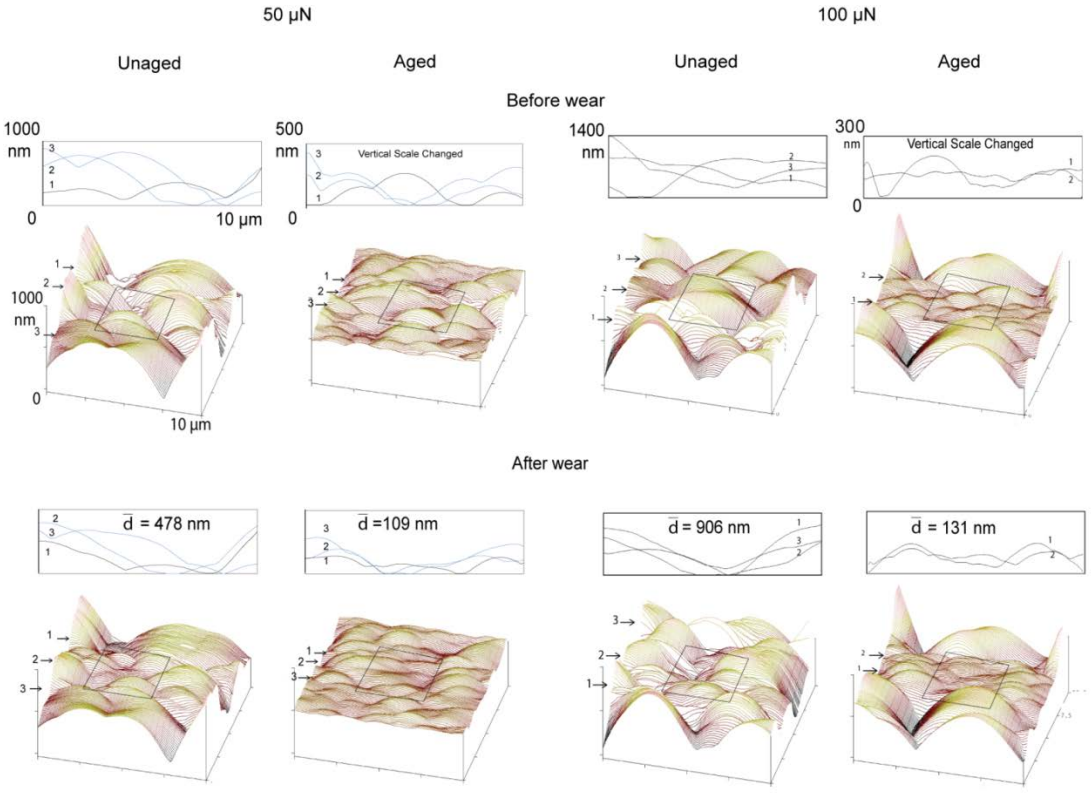

Fig. 3.4. Surface height maps and sections of unaged and aged cathodes showing worn region at 50 µN and 100 µN loads. Average wear depth ($\bar{d}$) are listed in the sections.

For the aged cathode in **Fig. 3.4** a flattening effect can be seen where the particles that were asperities are now more compressed into the substructure of the cathode. The unaged cathode observed from the particle behavior after wear was more easily ploughed and rearranged when compared to the aged cathode. Significant ploughing was observed for the unaged cathode under 150 µN load. The particle with uniform asperity was ploughed through the center and the after line map showed a valley created. When comparing the effect of doubling the load on both the unaged and aged cathodes, the

unaged cathode responded with a 90% increase in the wear depth whereas for the aged cathode wear depth only increased by 20%. This is believed to be due to higher hardness of the aged cathode.

3.3.3 Nanoscratch experiments

Nanoscratch experiments were conducted to determine the failure mechanisms present in the unaged and aged cathodes. **Fig. 3.5** shows nanoscratch results obtained for unaged and aged cathodes and nanoscratch on silicon for reference. The coefficient of friction as a function of normal load was plotted. At low load coefficient of friction was constant, at a certain load the coefficient of friction increased rapidly. The load at which this rapid increase in coefficient of friction occurs is known as the critical load (Bhushan, 2013). The critical load shows the load at which the surface of the cathode yields and plastic deformation occurs. The critical loads for unaged and aged are 120 and 175 μN, respectively (**Table 3.1**). The arrows in the height images show visible damage to the cathodes which occur as a result of plastic deformation and fracture. The aged cathode appears to be more scratch resistant than the unaged due to the higher hardness. However, the aged cathode breaks up catastrophically which appear to be in a brittle mode at loads higher than 175 μN.

Nanoindentation and nanowear experiments were performed by Chen et al. (2009) on Ni-Sn alloy coating for Li-ion battery study. Crack formation was observed during wear experiment and these were proposed to be similar observation of surface damage to

that of anode during charge-discharge cycling. The sliding contact stresses were proposed to be similar to the stresses due to the phase change of the anode during charge-discharge cycling.

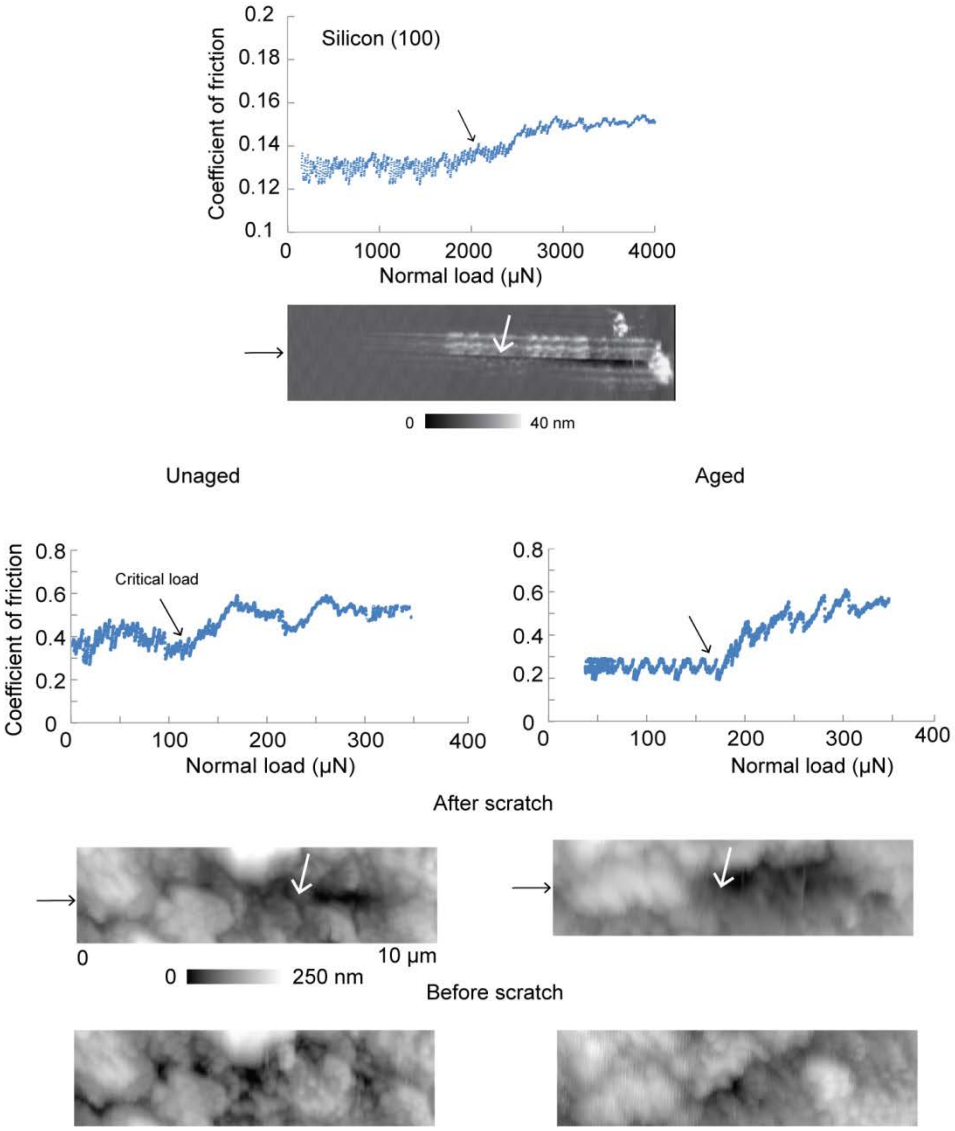

Fig. 3.5. Friction force as a function of load for unaged and aged cathodes and silicon (100) for reference. Coefficient of friction values obtained from the slope of the curves are also presented.

3.3.4 Nanofriction experiments

The nanofriction experiments conducted (**Fig. 3.6**) show that friction force of unaged and aged cathodes increased linearly with applied load. At any given load the friction force of the unaged was higher than the aged. The coefficient of friction was measured as the slope of the friction force versus applied normal load. The coefficient of friction values are shown in **Table 3.1 and Figure 3.6**. The coefficient of friction for the unaged cathode is found to be 0.42 and for the aged cathode 0.30. This is due to the higher hardness of the aged cathode.

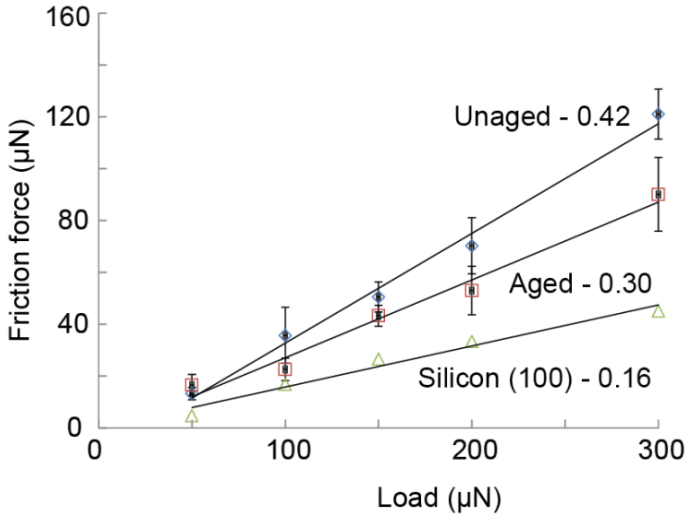

Fig. 3. 6. Friction force as a function of load for unaged and aged cathodes and silicon (100) for reference. Coefficient of friction values obtained from the slope of the curves are also presented.

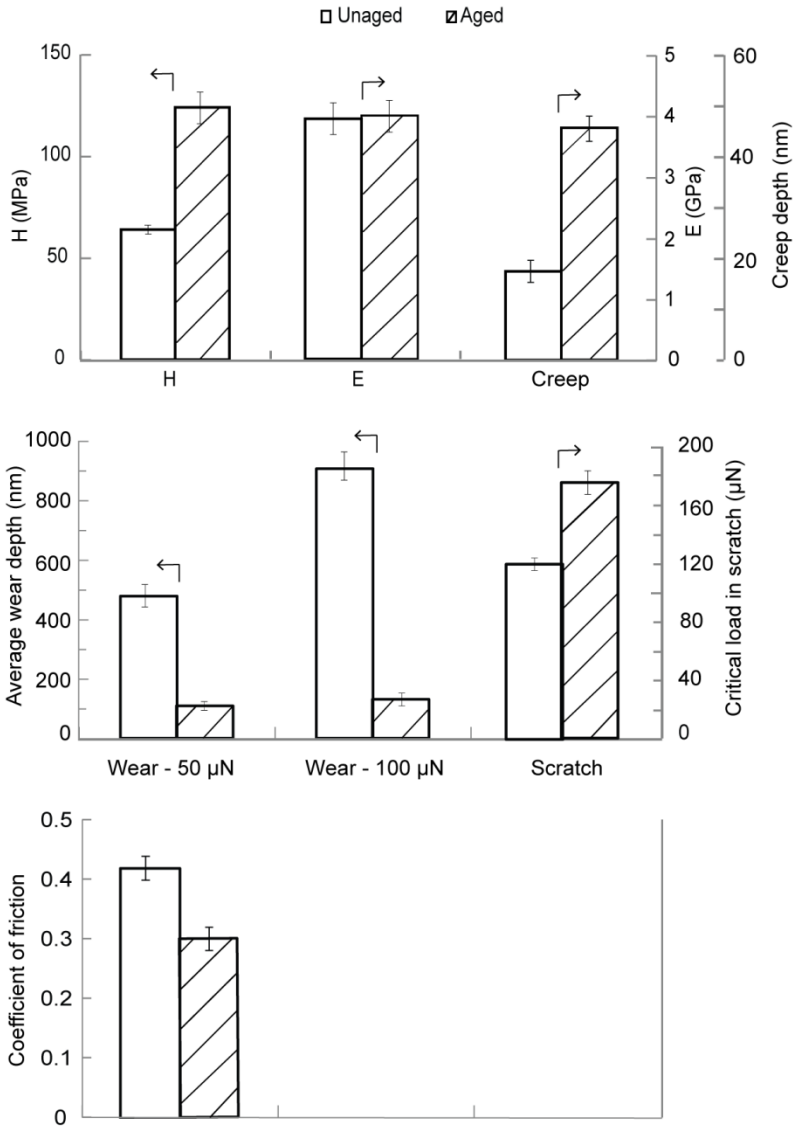

Fig. 3.7. Bar chart showing hardness (H), elastic modulus (E), average creep depth, average wear depth at 50 μN and 100 μN loads, critical load in scratch and coefficient of friction of unaged and aged cathodes.

3.4 Summary and Outlook

Coarsening and agglomeration of $LiFePO_4$ nanoparticles have been observed during aging, which is expected to increase residual stresses within the cathode. Nanomechanical characterization and mechanical integrity studies were carried out to determine the effect of change in physical and chemical properties and the increase in internal stresses during aging. Measured nanomechanical properties include hardness, elastic modulus, and creep, while mechanical integrity properties include of unaged and aged $LiFePO_4$ battery cathodes nanowear, nanoscratch and nanofriction. Data are summarized in **Fig. 3.7**. The aged cathodes shows higher hardness, creep depth and critical load in scratch and lower wear depth and coefficient of friction. Higher hardness in the aged cathodes is believed to make it brittle and during scratch test, catastrophic damage is observed. Increase in creep depth is believed to be due to the binder degradation during aging.

Chapter 4: In situ AFM electrochemical characterization of Li-ion battery cathodes

4.1 Introduction

Li-ion batteries have long been studied and developed as a power source for portable devices (Armand and Tarascon, 2008). Since the early 2000s, Li-ion batteries have emerged as energy storage media for electric vehicles (EV), hybrid-EV (HEV) and plug in-EV (PHEV) in order to reduce the dependence on non-renewable energy sources. EVs are environmentally friendly because of their lower carbon emissions, and they are more economical to operate than conventional automobiles. Li-ion batteries are used in the automotive industry because of their extended life cycle, and because of their high energy density per unit weight (specific energy) (Nagpure and Bhushan, 2009; Nagpure, 2011).

Padhi et al. (1997) first introduced lithium iron phosphate ($LiFePO_4$) as a Li-ion battery chemistry for cathode material. The $LiFePO_4$ cathode has been of interest to researchers because of its coulometric capacity[1] per unit weight (≈170 mAh g^{-1}), high thermal stability, specific energy (≈ 0.60 Wh g^{-1}), and low toxicity (Borong et al., 2011; Choi et al., 2012; Zaghib et al., 2013). $LiFePO_4$ is a viable option for meeting the

[1] The total Amp-hours available when the battery is discharged at a certain discharge current from 100% state-of-charge to the cut-off voltage. Capacity is calculated by multiplying the discharge current by the discharge time.

requirements set by the United States Advance Battery Consortium (USABC) for the EV (Anonymous, 2002, 2006a, 2006b). Over time, electrochemical properties of Li-ion batteries degrade, which leads to a reduction in storage capacity. Therefore, understanding the underlying mechanisms of the aging phenomenon in Li-ion batteries is of paramount importance in order to extend the life of Li-ion batteries (Nagpure, 2011; Nagpure et al., 2013).

Numerous ex-situ studies have been conducted to study the aging phenomenon in Li-ion batteries. These studies include atomic force microscopy (AFM), scanning electron microscopy (SEM), transmission electron microscopy (TEM), Raman spectroscopy, and other X-ray and neutron techniques (Nagpure, 2011; Nagpure et al., 2013). These ex-situ studies were conducted by comparing the aged and unaged materials of cathodes and anodes in order to reveal morphological, electrical, and structural changes that occur during cycling. More specifically, studies on the $LiFePO_4$ battery cathode showed that $LiFePO_4$ nanoparticles agglomerate with age. The carbon coating on the particle needed for conductivity might degrade during agglomeration. Agglomeration is believed to result in an increase in surface resistance and a decrease in surface conductivity, which consequently reduces battery capacity (Nagpure et al., 2009, Nagpure, 2011; Ramdon and Bhushan, 2012). Nanomechanical characterization experiments have been conducted to observe the effect of increased internal stress during aging (Ramdon and Bhushan, 2013). Increases in creep and hardness were found to be associated with the degradation of the PVDF binder and the formation of a dislocation due to the high internal stress and strain created during lithiation and delithiation.

Although ex-situ studies resulted in some understanding of the aging phenomenon, a real time investigation of the battery electrodes during cell operation is only possible through in situ techniques.

In order to conduct in situ electrochemical measurements, custom built electrochemical cells that can operate inside an instrument must be utilized. Each experimental technique has its own set of difficulties associated with their operating conditions. For example, SEM and TEM require the sample to be in a vacuum, while AFM requires an open cell design that allows access to the electrode being investigated. AFM allows for the direct observation of the morphologies of Li-ion based electrodes at high resolution and on a nanometer scale (Vidu et al., 2002; Campana et al., 2005; Doi et al., 2008; Park et al., 2013).

In this chapter, a review of various in situ electrochemical cells used during Li-ion battery investigations is presented (Ramdon et al., 2013). Reasons for selecting AFM techniques are given. Different electrochemical cell designs used for in situ AFM experiments are described. Then a two-electrode electrochemical cell design is proposed, and the results of in situ AFM electrochemical studies on a $LiFePO_4$ battery cathode are presented.

4.2 Review of In situ electrochemical cells

Various in situ techniques have been applied to the study of Li-ion batteries, including optical, electron, AFM, neutron and X-ray techniques. Table 1 presents a

summary of design requirements and comments on different electrochemical cells for each experimental technique. Schematics of cell designs are shown in **Fig. 4.1(a)** to **4.1(c)**. The following is a more detailed discussion of each technique and the in situ electrochemical cells utilized.

4.2.1 Optical

Optical methods include Raman microscopy and optical microscopy, which require a top cover that allows light to pass through, as shown in **Fig. 4.1(a).**

The Raman microscope technique is desirable for studying the structural and chemical composition of a sample. A Raman microscope is extremely useful for studying carbonaceous material, and it is useful for studying lithium intercalation through the carbon coating of cathodes (Panitz et al., 2001). Li^+ extraction and insertion has been observed on $LiNi_{0.8}Co_{0.15}Al_{0.05}O_2$ cathodes (Lei et al., 2005). The electrochemical cell used in this experiment was designed with a glass top cover to allow monochrome light to pass through. Panitz et al. (2001) had a similar electrochemical cell design. They reported that when the thickness of the electrolyte layer was reduced from 0.5 mm to 0.2 mm, it resulted in an improved optical efficiency.

Though the optical in situ technique can only be utilized to probe morphological changes on the surface of the cathode, it does provide resolution on a micron scale (Chen et al., 2011). An electrochemical cell utilized for the in situ optical microscopy technique is given in **Fig. 1(a).** Harris et al. (2010) used the color change of graphite as an indicator

of the extent of lithiation in order to obtain spatial profiles of Li intercalation. Quartz upper glass was used, however it was stated that lithium degrades the quartz material and a sapphire glass would yield better results.

4.2.2 Electron

The electron microscope can observe morphological changes on the nanometer scale. It requires an electrochemical cell with a transparent window to an electron beam. The experiments are conducted in a high vacuum and require electrolytes that are compatible, such as ionic liquids and solid electrolytes.

In situ TEM has been limited by the requirement of having ultra-thin samples (~100 nm thickness) and a focused ion beam (FIB). TEM provides morphological, structural and compositional information using the techniques of imaging, diffraction and spectroscopy respectively (Meng et al., 2011). Brazier et al. (2008) were the first to conduct an ex-situ TEM observation of a solid state Li-ion battery. The first significant in situ electrochemical cell design was created by Lui and Huang (2011) (also see Lui et al., 2012), which used ionic liquid electrolytes (ILEs). These electrolytes were shown to perform better in a high vacuum because of their ultra-low vapor pressure. Unocic et al. (2012) created an in situ electrochemical cell that used a MEMS-based biasing microchip platform to seal the highly volatile electrolyte between two transparent electron SiN_x membranes. In order to improve spatial resolution, an energy-filtered transmission

electron microscope (EFTEM) (to minimize chromatic aberrations) was used, followed by an electron energy loss spectroscope (EELS) to determine chemical changes.

In situ SEM studies were first performed by Orsini et al. (1998). Their electrochemical cell design did not allow for the cycling of the cell inside the SEM, thus the cycling was done outside of the SEM. After cycling, the cell was cooled down to -20^0C to pause the electrolyte degradation process, and then it was transferred to the SEM in an air-tight container. Raimann et al. (2006) designed an electrochemical cell to have the least amount of evaporation of the electrolyte as possible by moderating the size of the exposed working electrode (pinhole diameter), the amount of electrolyte used, and the vacuum level inside of the SEM. However, this method reduced the resolution due to the scattering of electrons in the gas atmosphere that was created as the electrolyte evaporated. The problem faced when using conventional liquid electrolytes was eliminated (Chen et al., 2011) by using ionic liquids, which are very stable even in ultra-high vacuums because of their very low vapor pressure.

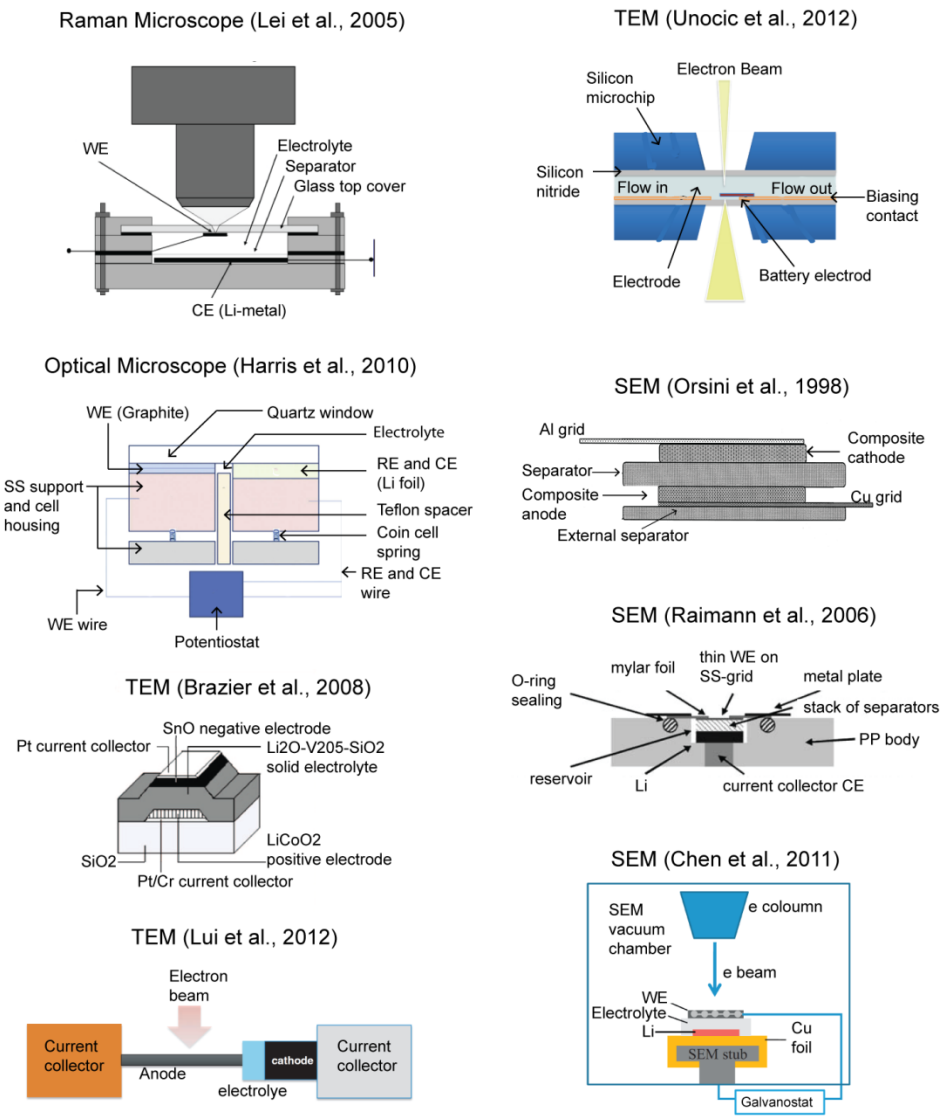

(a)

Continued

Fig. 4.1. Schematics of In situ electrochemical cells for (a) Raman, optical and transmission electron microscope (TEM) and scanning electron microscope (SEM), (b) AFM, and (c) for neutron and X-ray experimental techniques. WE, CE and RE represent working electrode, counter electrode and reference electrode respectively.

Figure 4.1 continued

AFM

(Vidu et al., 2002)

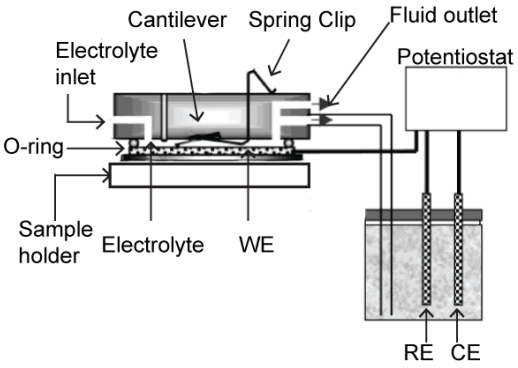

(Inaba et al., 2011)

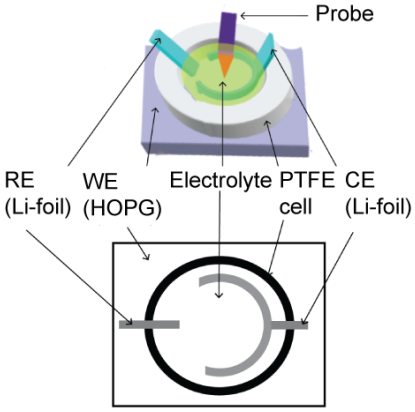

(Campana et al., 2005)

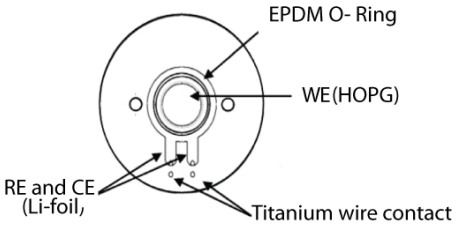

(Park et al., 2013)

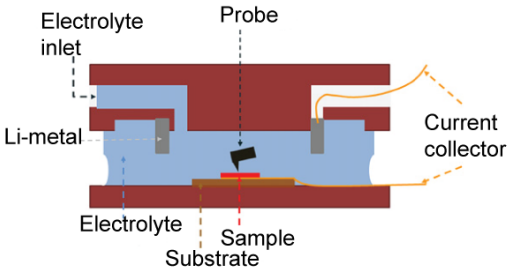

(b)

Continued

Figure 4.1 continued

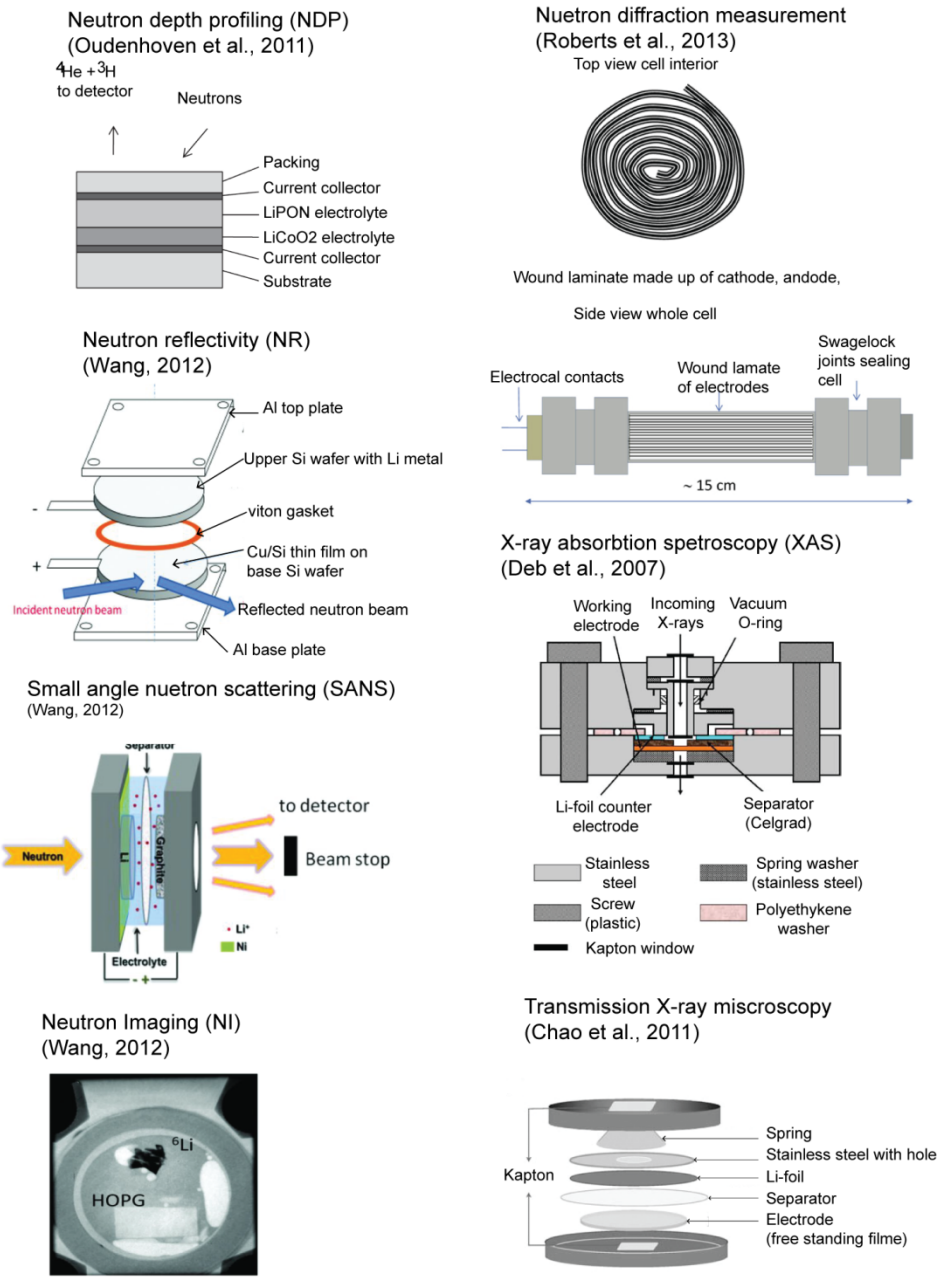

(c)

4.2.3 AFM

The AFM microscope is a versatile tool for studying Li-ion batteries because high resolution images of the cathode surface can be obtained. Experiments can be completed under ambient conditions, but an inert atmosphere for electrochemistry is required. Electrochemical cell designs used during in situ AFM electrochemical studies on Li-ion batteries have very specific requirements to ensure good performance. Open access from the top of the cell is required to allow the AFM cantilever to enter into the cell and onto the working electrode. The materials used must not be reactive with the components of the cell. For example, because the electrolyte is very reactive, cell component materials that are chemically resistant are required such as Teflon®, which is often used in cell fabrication. The cell needs to be designed to accommodate the electrodes. The cell's counter and reference electrodes must be placed at precise locations that have stable electrical connections to the potentiostat.

Cells containing three-electrodes and two-electrodes with a continuous flow and a static electrolyte have been used. Vidu et al. (2002) proposed a three electrode continuous flow electrochemical cell with the counter and reference electrodes located in an external reservoir, and with the working electrode located in the cell, as shown in **Fig. 4.1(b)**. This entire setup is in an argon environment. Park et al. (2013) used a different continuous flow cell than Vidu et al. (2002). In their design the lithium metal counter electrode was inside the electrochemical cell and the cell contained two electrodes (Park et al., 2013). Campana et al. (2005), and Doi et al. (2008) (also see Inaba et al., 2011)

used a non-flow electrolyte and three-electrode systems in which the counter and reference electrodes were placed in an enclosed cell. The area of the working electrode was confined by an O-ring, which prevented the electrolyte from leaking.

4.2.3 Neutron techniques

There are several neutron techniques shown in **Fig 4.1(c)**. Techniques include neutron depth profiling (NDP), neutron reflectivity (NR), small angle neutron scattering (SANS), neutron imaging (NI), and neutron diffraction. These techniques require an electrochemical cell that is transparent to energy particles, and that can be used to quantify the Li distribution and transportation within the battery.

NDP is a powerful technique for measuring Li-ion concentration deep in the sample. Oudenhoven et al. (2011) developed an in situ electrochemical cell for NDP applications that is shown in **Fig. 4.1(c).** This cell design requires heating the electrolyte to 250^0C, then maintaining this temperature for 10 min in order to reduce the resistance to the electrolyte at the interface by a factor of 2. This cell design is similar to that of Neudecker et al. (2000). Neutron reflectivity (NR) is most notable for measuring volume expansion and retraction on electrodes, as stated by Wang et al. (2012). The intensity of the NR is measured as a function of the momentum transfer. The electrochemical cell shown in **Fig. 4.1(c)** uses Li-metal in the counter and reference electrodes. Its electrolyte is enclosed by a Viton® O-ring that also confines the working electrode. Gold foil is used to make connections to the electrodes.

Small angle neutron scattering (SANS), shown in **Fig. 4.1(c)**, measures the neutron scattering intensity as a function of the momentum transfer velocity (Wang et al., 2012). This instrument is notable for measuring the structural variations in a sample. Li-metal is used in the reference and counter electrodes. The working electrode is comprised of graphite. The cell is also designed with quartz windows on the top and bottom to allow the neutron beam to pass through the cell.

Neutron Imaging (NI) shown in **Fig. 4.1(c)**, measures the spatial changes in the transmission of Li relative to a reference (Wang et al., 2012). NI may help to construct more accurate circuit models when designing rechargeable batteries in the future. Neutron diffraction measurements are performed on a specially designed electrochemical cell that contains a wound cathode, an electrolyte, and an anode sealed in a quartz or aluminum tube (Roberts et al., 2013). This was chosen to allow for a constant path length for neutron absorption.

4.2.4 X-ray techniques

X-ray absorption spectroscopy (XAS), shown in **Fig. 4.1(c),** is used for the monitoring of the structural composition of an electrode. This is the preferred technique for obtaining detailed information on electronic structure and order (Deb et al., 2004, 2007). The cell is completely sealed, thus allowing monitoring for an extended period of time. A Kapton® foil is used as the window in this cell design because the window must be transparent to X-rays. A transmission X-ray microscope is used for studying structural

and phase compositions. The in situ cell is made in a manner similar to a coin cell, however there is a hole through the top and bottom cover of the in situ cell that is sealed with Kapton® (Chao et al., 2011).

4.2.5 Selection of the technique used in the present study

AFM was selected for this study because it does not require samples to receive any special treatments that could cause changes or damage, such as the conductive coating required in electron microscopy. AFM does not require an ultra-high vacuum environment to operate. Conventional electrolytes, such as a hexafluorophosphate ($LiPF_6$) salt in an alkaline carbonate solvent, can be used. AFM provides high resolution morphological information for samples, and it can perform well in a liquid environment.

Table 4.1 In-situ electrochemical cell for studying Li-ion batteries

In-situ cell	Design requirement	Comments
Optical	Top cover plate transparent to visible light	
Raman microscope (Lei et al., 2005)		Structure and chemical composition at ~ 2 μm spatial resolution
Optical microscope (Harris et al., 2010)		Only shows morphological changes on microscale, low resolution
Electron	Window transparent to incoming electron beam. High vacuum required which limits electrolyte selection	Morphological changes on nanoscale can be measured
TEM (Brazier et al., 2008)		
(Lui et al., 2012)		
(Unocic et al., 2012)		Cross section observation can be made. Sample used must be thin down to 100 nm thickness (FIB required)
SEM (Orsini et al., 1998)		Battery cannot be cycled in SEM
(Raimann et al., 2006)		Uses a lower vacuum (<10 Torr) than normal SEM which allowed use of electrolyte
(Chen et al., 2011)		Uses an ionic fluid which has low vapor pressure. Assemble of cell aided with nanomanipulator.
AFM	Clear path for access with probe	Can be used in ambient, however inert atmosphere required.
(Vidu et al., 2002)		Continuous electrolyte flow. Reference and counter electrode outside of cell
(Campana et al., 2005)		
(Inaba et al., 2011)		
(Park et al., 2013)		Continuous electrolyte flow with reference and counter electrode inside cell
Neutron	Window transparent to energy particle	Can quantify Li distribution and transport in battery during operation
Neutron depth profiling (NDP)		Can measure Li concentration within the electrodes of the cell. To reduce resistance, the cell is heated before initial experiment.
Neutron reflectivity (NR) (Wang, 2012)		Measures neutron reflectivity intensity as a function of momentum transfer.
Small angle neutron Scattering (SANS) (Wang, 2012)		Notable for measuring the structure variation in a sample through neutron scattering intensity
Neutron imaging (NI) (Wang, 2012)		
Neutron diffraction (Roberts et al., 2013)		Wound cathode, electrolyte and anode stack
X-ray	Window transparent to X-ray	Can monitor detail structural changes
X-Ray Absorption Spectroscopic (XAS) (Deb et al., 2004) (Deb et al., 2007)	Kapton X-ray window	Completely sealed cell allows prolong monitoring. Provides detailed information on electronic structure and ordering.
Transmission X-ray Microscope (Chao et al., 2011)		Can study structure and phase composition

4.3 Experimental details

The proposed experimental cell was placed inside a glove box with an argon atmosphere. It was cycled using a potentiostat. During cycling, AFM was used to investigate any morphology changes.

4.3.1 AFM, glove box and potentiostat

Figure 4.2(a) shows the schematic of the Agilent 5500 AFM head (Agilent Technologies, Chandler, AZ). The main components of the AFM head are a laser diode, a piezo scanner, a cantilever, and a quad diode laser detector (Bhushan, 2011). The sample is mounted under the AFM head below the cantilever. The cantilever tip assembly is mounted to the lower end of the peizo scanner. The piezo scanner consists of three separate electrodes that precisely scan the sample in the x-y plane in a raster pattern and that move the sample in the vertical (z) direction. A sharp tip at the free end of the cantilever is brought into contact with the sample. Features on the sample surface cause the cantilever to deflect in vertical and lateral directions as the peizo scans the tip over the surface. A laser beam from a laser diode is directed onto the back of the cantilever near its free end, tilted downward at about 9 º with respect to the horizontal plane. The cantilever is coated in gold on the detector side to enhance laser reflection. The reflected beam from the vertex of the cantilever is directed onto a quad diode laser detector.

Topographic features of the sample cause the tip to deflect in a vertical direction as the sample is scanned under the tip. This tip deflection will change the direction of the reflected laser beam, thereby changing the intensity difference between the top and bottom sets of the diode laser detectors (AFM signal). A feedback circuit is used to modulate the voltage applied to the piezo scanner and to adjust the height of the piezo. This feedback system ensures that vertical deflection from the cantilever (given by the intensity difference between the top and bottom detector) remains constant during scanning. The feedback signal is used to create the AFM height image, while the raw deflection signal creates the deflection image. The deflection image provides a good lateral resolution for particles or other features, and the height image gives accurate height information.

A balanced pendulum method is used as part of the design of this AFM head. This means the laser diode, piezo and cantilever are all fixed together and move as a balanced pendulum. This allows the laser tracking spot to remain fixed onto the cantilever. Other AFM systems use a lens system to track the laser spot on the cantilever while the cantilever moves independently. This causes artifacts at the end of large scan size images. The balanced pendulum design also lowers the moment of the inertia on the piezo, thus reducing noise in the system.

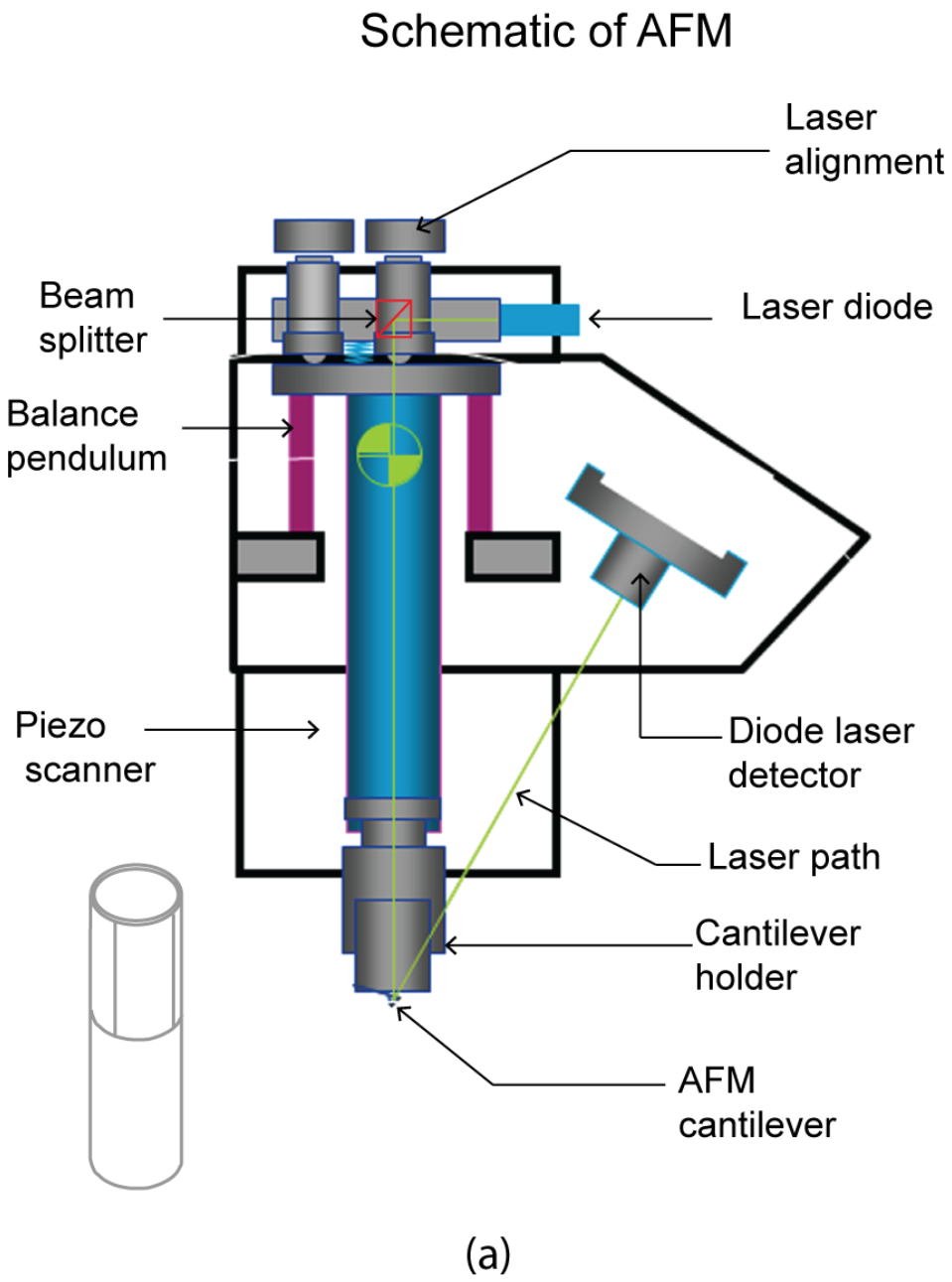

Continued

Fig. 4.2. Schematics of (a) AFM and (b) glove box designed for storage as well as electrochemical experiments.

Figure 4.2 continued

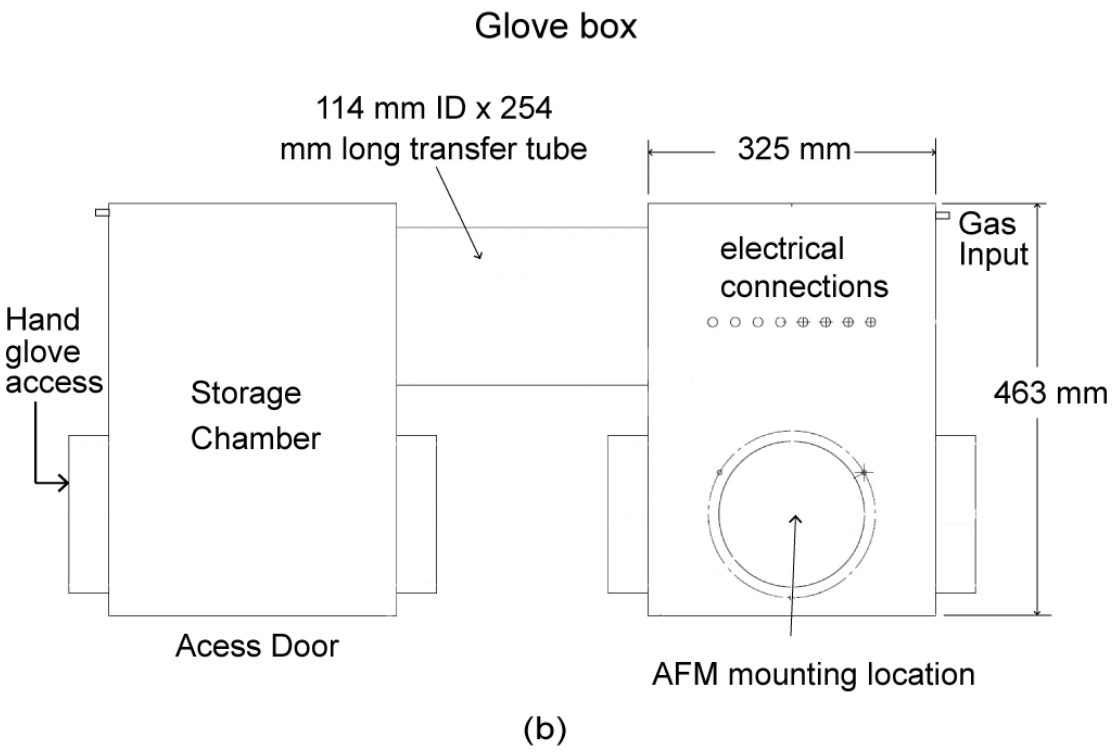

(b)

The glove box used, shown in **Fig 4.2(b),** is designed with two compartments: one compartment for storage is on the left and the other compartment for in situ AFM electrochemical experiments is on the right. They both are independently sealed with a transfer chamber in between, which allows for the transfer of items to and from storage while performing experiments. The glove box has ports used to connect the electrical connections to the potentiostat for cycling. The AFM is mounted through a circular hole at the top, which provides a good seal for the argon environment. In situ experiments were conducted in an ultra-high purity argon (99.998%) filled glove box maintained at a slightly positive pressure (~ 10 Pa), and equipped with drierite moisture absorbent

material (W.A. Hammond Drierite. CO. LTD, Xenia, OH). The potentiostat used is the Gamry Reference 600 (Gamry Instruments, Warminster, PA).

4.3.2 In situ cell design

As presented earlier, three-electrode and two-electrode cell designs have been used in previous work. In these studies the three-electrode cell design has separate counter and reference electrodes and the two-electrode cell design has the same electrode for both counter and reference electrodes.

The schematic of a three-electrode cell is shown in **Fig. 4.3(a)** top. The working electrode (WE), reference electrode (RE) and counter electrode (CE) as well as the electrolyte and the potentiostat electrical connection are shown. The WE is typically where the sample is tested, it is where the potential is controlled, and where the current is measured. The RE is used in measuring the WE electrode potential and it is normally kept at a constant electrochemical potential. The CE completes the circuit. The current flowing through the solution enters through the WE and leaves through the CE.

For in situ AFM electrochemistry, an open cell design is needed to perform AFM imaging. A three-electrode commercial electrochemical cell design (Agilent N9410A-OC-LIQUID) is shown in **Fig. 4.3(a)** bottom. The working electrode has a confined area for the electrolyte using an O-ring and a spring loaded pin and clip mechanism. The cell is designed to accommodate a rigid wire of about 0.5 mm in diameter for the counter and reference electrodes. In the case of Li-ion batteries, Li-metal is needed for the counter

and reference electrodes. Li-metal is soft, and since it is not rigid it will not remain in place. Furthermore, this cell design has a shallow reservoir, so the electrolyte will evaporate in a shorter time than the experiment duration of several hours.

To simplify the assembling process of the cell in the glove box, a two-electrode setup is used as shown in **Fig. 4.3(b)** top. The schematic of the proposed in situ AFM electrochemical cell is shown in **Fig. 4.3(b)** middle and bottom. The Li-wire cell design shown in **Fig. 4.3(c)** middle is a modification of the design discussed earlier. It uses a deeper cup to hold larger quantities of electrolyte, and it has an opening which allows for the easy insertion of the flexible Li-wire without obstructing the AFM head. It uses counter and reference electrodes consisting of Li-wire, and it uses a Li-ion cathode as the working electrode submerged in an electrolyte. A Teflon® cup with a hole through the side (~ 3 mm) for the Li-wire is used. A copper metal rod with a plate for mounting the sample is placed through the base of the cup, and it is sealed by a Viton® O-ring. The inner diameter of the cell opening is 30 mm and 8 mm in depth.

The other design is a coin cell design as shown in **Fig. 4.3(d)**. It uses a Li-foil with an opening in the middle as the reference and counter electrode. The working electrode is separated from the Li-foil with a separator. The cell components are assembled in the lower cell casing with a spring and spacer below the working electrode used for making an electrical connection from the working electrode to the lower casing of the cell. A few drops of electrolyte are dropped into the cell before another spacer with an opening is placed on top of the Li-foil. Then the top cover with an opening is

placed as the cover for the cell. This assembly is then crimpled shut in a crimping machine.

The wire AFM electrochemical cell in **Fig. 4.3(c)** was chosen to conduct the experiments. It does not have numerous parts or require the punching of separators and lithium, nor does it necessitate a crimping machine. Li-wire was used for the counter and reference electrodes. The Li-wire can be handled more easily in the glove box and it does not need additional preparation before the cell is assembled.

A description of the steps taken to assemble the cell follows. First the Teflon® cup with a copper metal rod through its base and the Teflon® O-ring are cleaned. These components are placed in a beaker that is then filled with isopropyl alcohol and sonicated for 15 minutes. Next the components are dried in an oven at 75 °C for approximately 12 hours. The components are then transferred to the glove box, which is purged three times with argon. A working electrode of about 15 mm in diameter that was cut from a commercial battery cathode is affixed to the copper plate at the top of the copper rod. The working electrode is attached using an oversized Teflon® O-ring in order to keep it in position. An electrolyte of 1M $LiPF_6$ salt in 1:1 ethylene carbonate/dimethyl carbonate (Novolyte technologies, Zachary, LA) was used to fill the cell to ¾ capacity (about 4 cm^3), allowing room for the AFM probe and preventing spillage.

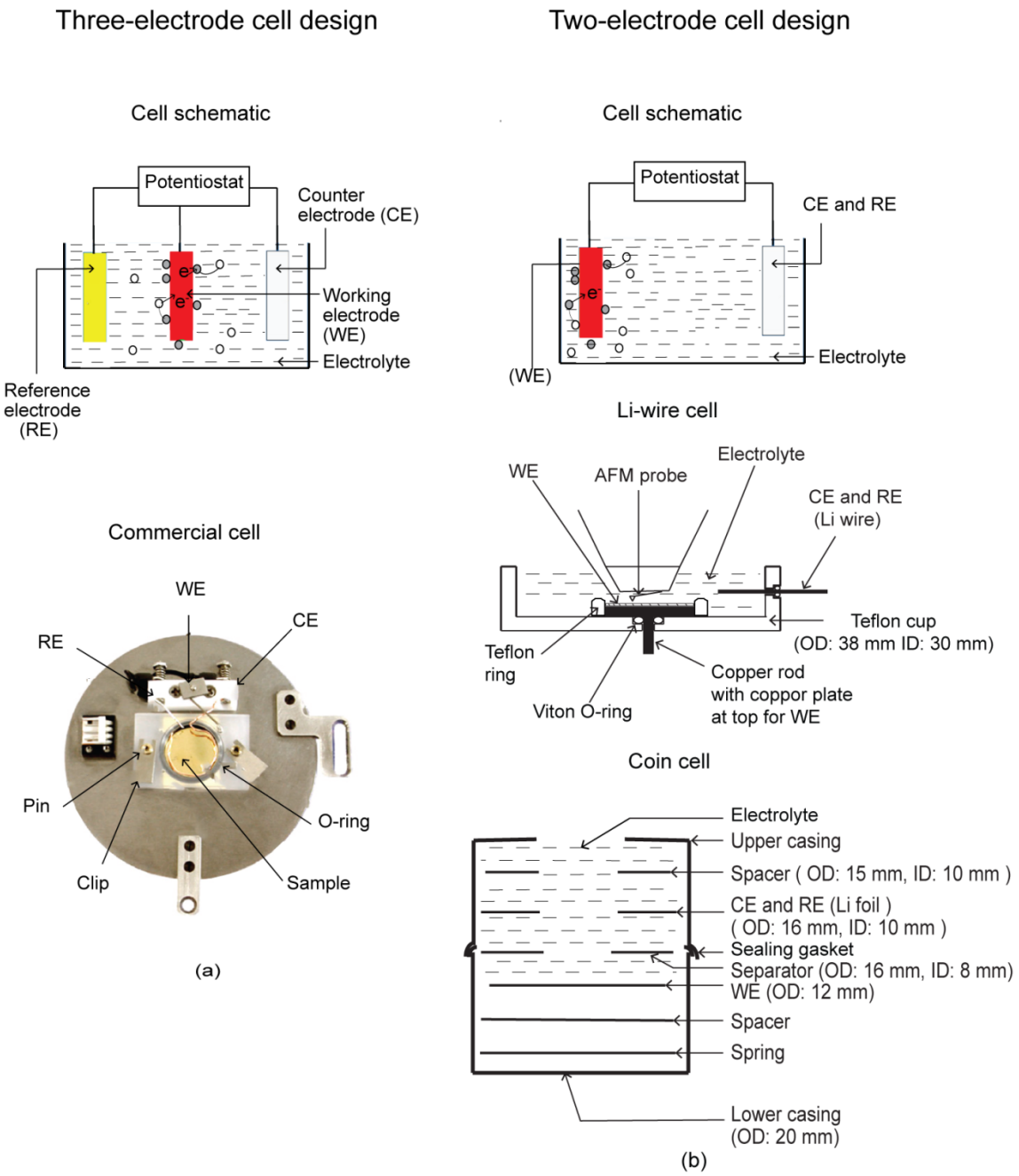

Fig. 4.3. AFM electrochemical cell designs proposed for in situ electrochemical experiments, (a) three-electrode with cell schematic (top) and commercial cell (bottom), and (b) two-electrode cell design with cell schematic (top), Li-wire cell (middle) and coin cell (bottom).

4.3.3 Extraction of samples from a commercial cell

Cylindrical Li-ion cells used in the experiments have cathode material on an aluminum current collector made of $LiFePO_4$ nanoparticles. These nanoparticles are coated with carbon for increased conduction. They are mixed in a slurry of polyvinylidene fluoride (PVDF), which acts as the binder. The graphite on a copper current collector is used as the anode, and lithium hexafluorophosphate ($LiPF_6$) salt in an alkaline carbonate solvent is used as the electrolyte. The anode and cathode are separated by a separator, and then rolled in a tube to create the cell. The cell has an operating voltage of 3.3 V and a nominal discharge capacity of 2.3 Ah.

The cell was charged and discharged completely at 1C (1C = 2.3 Ah) to verify its capacity. Next, the cell was disassembled in air, and long strips of cathode were extracted. One side of the extracted cathode was cleaned using 1-methyl 2-pyrrolindinone (Sigma Aldrich, St. Lous, MO) to remove $LiFePO_4$ and to expose the aluminum current collector.

4.3.4 A Commercial Cell for comparison

The commercial cell ANR26650 (A123 Systems, Inc, Waltham, MA) was used as a reference for data obtained from the experimental wire cell. It has a charge/discharge capacity of 2.5 Ah, and an operating voltage of 3.3 V. It was completely charged and discharged using the potentiostat at a charge/discharge rate of C/6. The current for a C/6

rate was obtained by dividing the charge/discharge capacity of 2.5 Ah by 6 to obtain ± 0.417 A. This C/6 rate was chosen to be similar to the rate used during the in situ AFM experiment in order to serve as a suitable reference.

4.3.5 In situ AFM experiment

The cell was cycled three times using a potentiostat, known as a formation cycle, before the start of the experiment. This was done to allow the cell to stabilize its charge/discharge capacity, as well as to develop a solid electrolyte interphase (SEI) layer. After the formation cycle, the in situ AFM experiment was conducted. Before the cell was charged AFM height and deflection images were taken, then after charging the cell by applying a positive current these images were taken again. The cell was then discharged by applying a negative current, and post discharge AFM images were taken. The AFM images were taken in contact mode using a silicon probe with a 70 nm thick gold reflective coating (Budget Sensor ContGD), a force constant of 0.2 N/m, and a resonant frequency of 13 kHz. An AFM scan speed of 2 Hz was used. AFM images were then processed using Agilent Pico Image Expert software, and particles were analyzed using the particle size analysis feature.

The theoretical capacity of the experimental wire cell is needed in order to set the C-rate used to cycle the cell. The C-rate is a measurement of the rate at which a cell is charged and discharged relative to its capacity. A charge rate of 1C means that it would take 1 h to charge the cell and 1 h to discharge the cell if it is discharged at a current of

2.3 A. In order to calculate the theoretical capacity of the experimental wire cell, the capacity per area (cm^2) of the original complete cell was calculated. This calculation was done by dividing the capacity specified by the manufacturer by the total area of the cathode material in the cell. The theoretical capacity of the cell can be calculated by multiplying the capacity per area by the area of the working electrode in the experimental wire cell. The capacity per area of the cathode is 1.189 mAh/cm^2(2.3 Ah/1935 cm^2). The theoretical capacity of the experimental cell is 1C ~ 1.96 mAh/cm^2 (1.189 mAh/cm^2 x 1.65 cm^2). A C/6 charge rate was chosen because it is an open cell and the electrolyte will evaporate over time. This rate will allow the AFM experiment to be completed without observing the effects of electrolyte evaporation. This theoretical capacity value was then divided by six to give the C/6 (± 327μAh) charge/discharge rate.

The Pico Image Expert image analysis software (Agilent Technologies, Chandler, AZ) was used to analyze the particle diameter. The software employs a specific algorithm to determine the peaks and the associated valleys for a particle. Then a segmentation method is applied to select the particle boundary. The selection can then be more precisely tuned, depending on the particle of interest, by changing the height threshold setting and the area of particle selection setting.

4.4 Results and Discussion

Experiments conducted on a commercial Li-ion battery that will serve as a reference for the in situ AFM wire experimental cell are presented. AFM images of the bare cathode and the cathode in an electrolyte are presented as a means of discussing the impact of the electrolyte on imaging. The cell was charged and discharged at a C/6 rate, which should take 6 hours to charge and 6 hours to discharge. In situ AFM images of the experimental wire cell during charging and discharging are also presented in order to study the morphological changes that occur.

4.4.1 Charge/discharge curves of the commercial cell and the Li- wire cell

The theoretical charge/discharge capacity of the commercial cell is 2.5 Ah, whereas the measured capacity of the battery was calculated to be 2.6 Ah. This was calculated by multiplying the applied current by the time taken to completely discharge the cell. This calculation was done to verify the manufacturer's rated capacity and to gauge the performance of the cell. The difference in capacities could be due to the lower and upper limits of the cell used by the manufacturer when determining the cell's charge/discharge capacity.

Charge and discharge curves were obtained on a commercial $LiFePO_4$ cell to provide a reference to that of the experimental wire cell. The charge and discharge curves are shown **Fig. 4.4**. The cell was charged from the lower limit of 2.5 V to the

upper limit of 4.2 V. During charging the voltage of the cell rapidly increased from 2.5 V to 3.29 V, where it increased steadily over 5.5 hours until the voltage reached 3.44 V, then it increased rapidly to the upper limit of 4.2 V. The discharge was then started immediately, with a beginning charge of 4.1 V. In **Fig. 4.4** the gap between the ideal starting discharge voltage and the voltage found in this experiment is represented by the dotted line, which shows where the voltage curve should have started in an ideal case. The voltage rapidly dropped to 3.28 volts, which is slightly below the operating voltage of the cell of 3.3 V. The cell then gradually discharged at a steady rate over 5.5 hours until it reached 3.1 V, at this point it decreased rapidly until reaching the lower limit of 2.5 V.

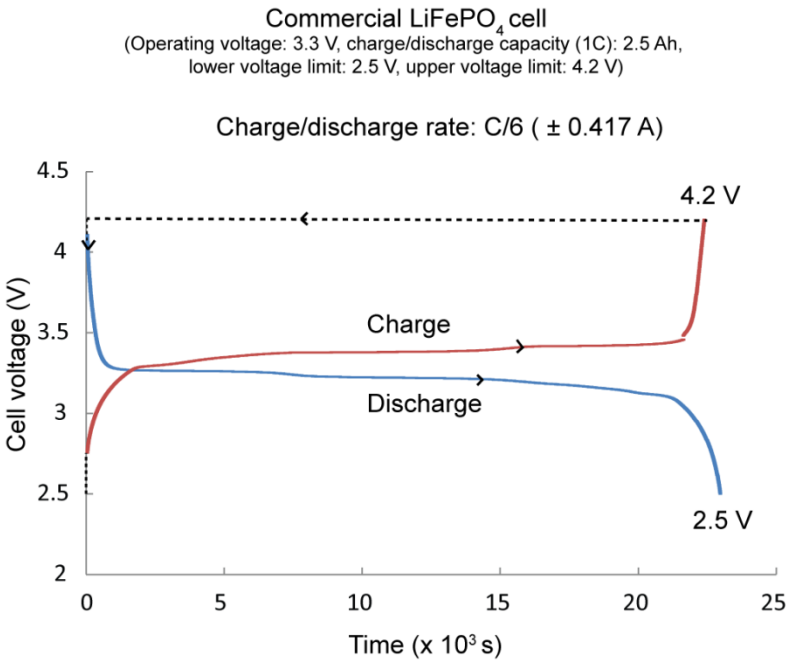

Fig. 4.4. Charge and discharge curve of a commercial $LiFePO_4$ cell.

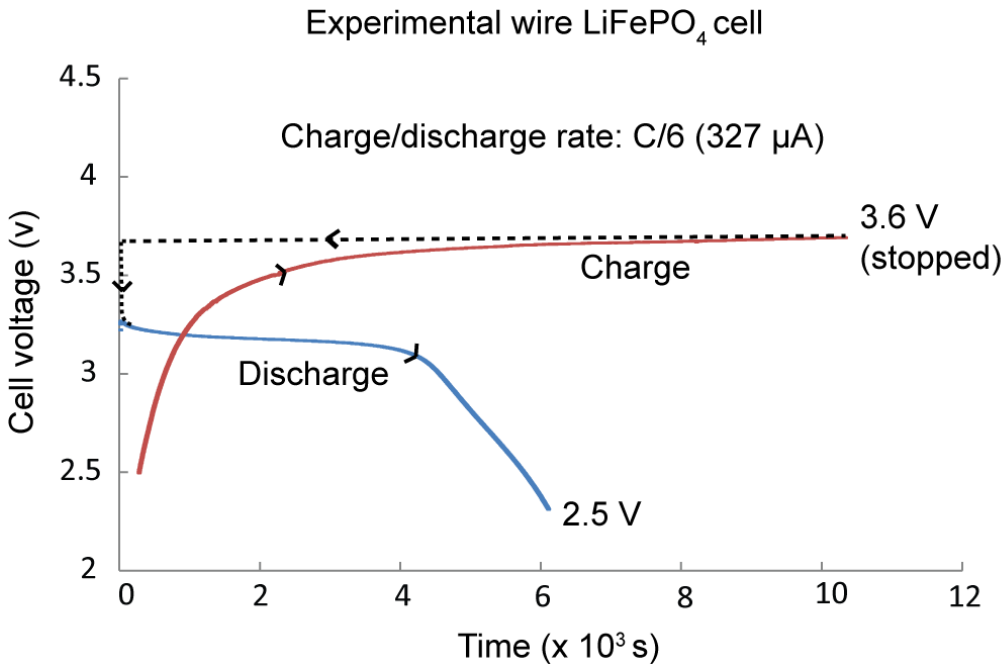

Fig. 4.5 Charge and discharge curve of an experimental wire $LiFePO_4$ cell.

The cycling of the Li-wire cell data are shown in **Fig. 4.5**. Based on the available lifetime limitation of the cell, it was stopped 2.7 hours into charging. The discharge of the cell reached the lower limit of 2.5 V in 1.7 hours. At the start of charging the cell the voltage increased gradually over 1 hour, and then it gradually leveled to the limit of 3.6 V for the remaining time. The discharge was started immediately after charging was stopped. The starting discharge voltage was 3.27 V. In **Fig. 4.5** the dotted line shows the drop in voltage from charging to discharging, and it shows where the discharge curve should have started in an ideal case. The cell's voltage reduced gradually to 3.1 V, and then reduced more rapidly to the set lower limit.

The commercial cell's charge and discharge curves were as expected from the theoretical calculations. The theoretical capacity was similar to the experimental capacity. The experimental wire cell showed a larger drop in voltage from the end of discharging to the start of charging, and discharging occurred much faster than the theoretically calculated discharge time. This result may be because the cell is open and the electrolyte volume in the cell is slowly reducing over time. Therefore, the concentration of the electrolyte is changing.

4.4.2. AFM Images of the bare cathode and the cathode in the electrolyte

Representative AFM images of the bare cathode and the cathode in the electrolyte are shown in **Fig. 4.6**. The AFM image of the cathode in the electrolyte is slightly noisier than that of the bare cathode. The boundary of the particles shown in the deflection image of the bare cathode is better defined than the particle boundary in the deflection image of the cathode in the electrolyte.

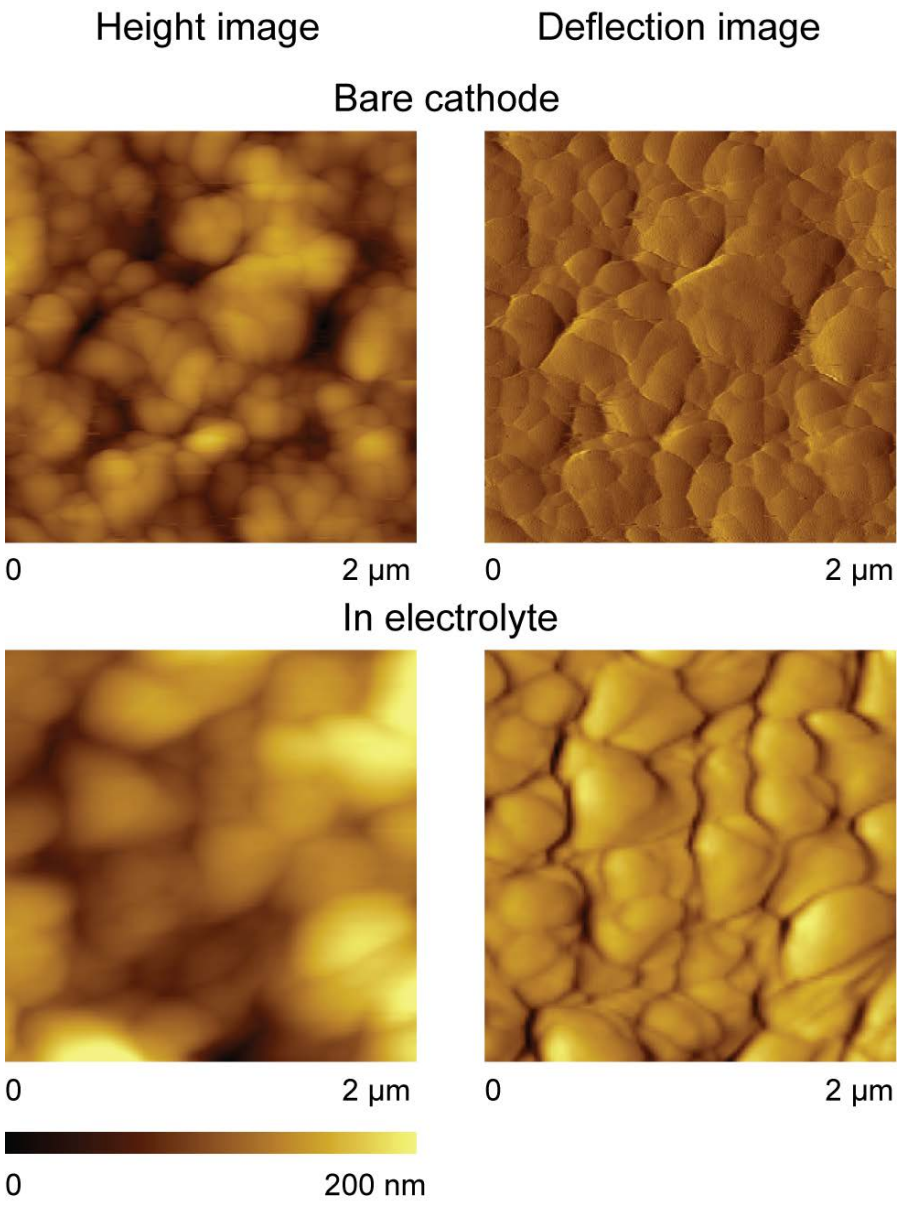

Fig. 4.6. AFM height and deflection image of bare and in electrolyte $LiFePO_4$ cathode.

4.4.3 In situ AFM images of cathode during charge and discharge

Fig. 4.7 shows height and deflection images, as well as the particle area analyses of the cathode, initially and after both charging and discharging. A visible change in the shape of the particles was observed in the images collected before and after charging. The particles became more rounded. After discharging the cell, the shapes of the particles became more similar to the shapes initially observed. The particles appear visually larger after discharging than after charging.

Particle analysis was then done to quantify the changes in the size of the particle, as shown in **Fig. 4.7.** The particle selected had a distinct shape and outline. The particle was also visually separate from the surrounding particles and had a distinct boundary. This selection process facilitates the proper selection of a particle by the image analysis software, and produces accurate results. The particle chosen was highlighted, and the area of the particle was determined from the software. The area of the initial particle chosen is 0.3 μm^2. After charging, the area of the particle was reduced to 0.26 μm^2. The cell was then discharged as shown in **Fig. 4.5,** and an image was taken. The particle size changed from 0.26 μm^2 to 0.33 μm^2 after discharging with a change on the order of 25%. This result shows that an increase in the size of the particle from fully charged to fully discharged exists. This increase is due to the phase change of the particle from the $FePO_4$ phase to the $LiFePO_4$ phase as described below.

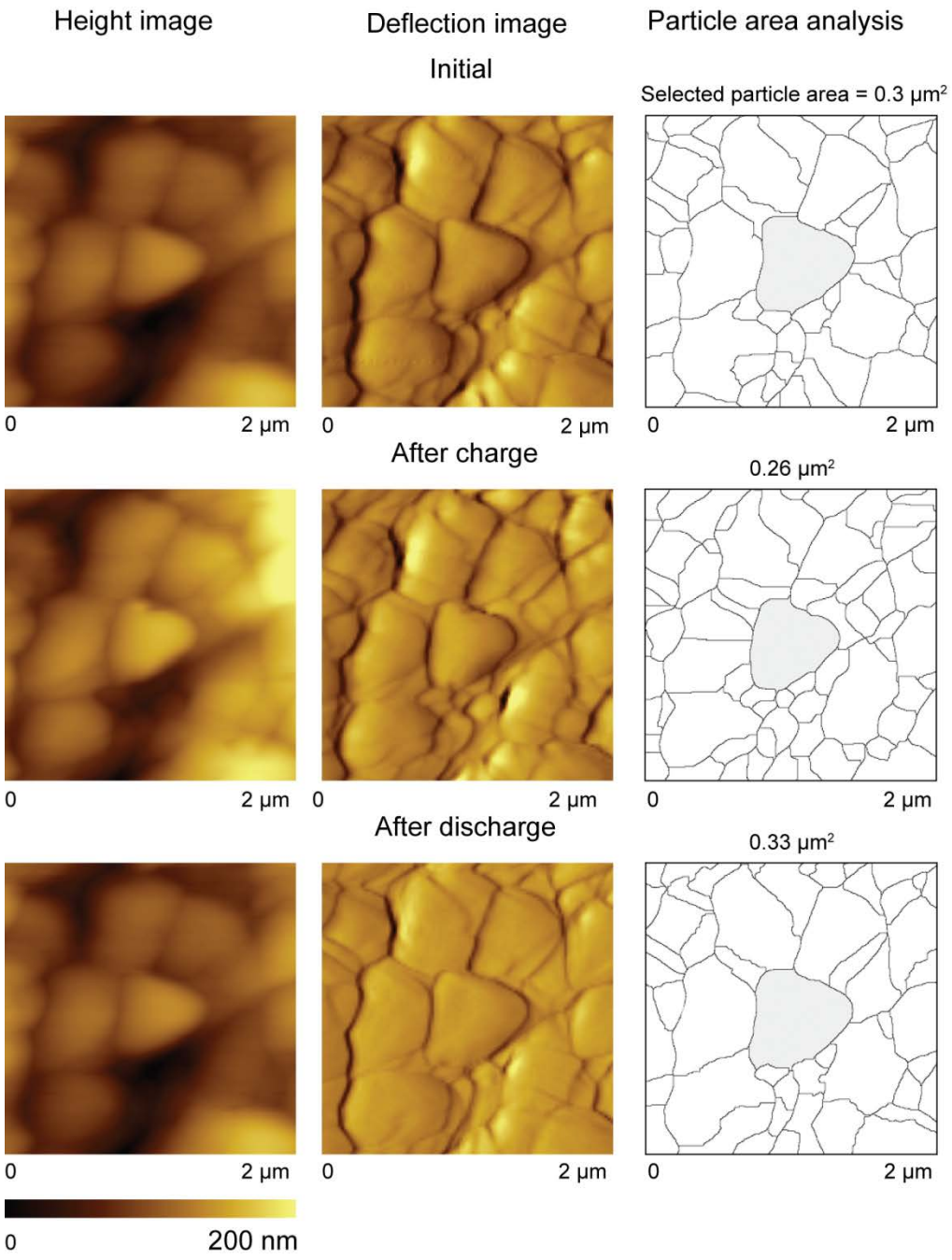

Fig. 4.7 AFM height and deflection image as well as particle area analysis of $LiFePO_4$ cathode showing change of particle size between charged and discharged states.

To understand what is occurring within the cathode as the cell is charged and discharged it is important to examine the morphological changes shown in **Fig. 4.7**. Srinivasan and Newman (2004) described this in the form of a shrinking core model. In a fully charged cell there exist single phase $FePO_4$ particles in the cathode. As the discharge is started, a reaction begins on the surface of the $FePO_4$ particle, and the Li^+ moves from the anode to intercalate into the cathode. The $FePO_4$ particle then changes to a $LiFePO_4$ particle. The Li^+ intercalates into the lattice of the $LiFePO_4$ particle, eventually creating phase segregation between the Li-rich region (outer shell) that has a high Li content and the Li-deficient region (inner core). As discharge continues, a greater amount of Li is inserted into the lattice, there it intercalates to the Li-deficient region. This eventually will change the entire particle into one Li-rich region. The particle will then be fully converted into $LiFePO_4$. The reverse occurs during charging. The total unit volume change between the $FePo_4$ phase and the $LiFePO_4$ phase is 6.8% (Phadi et at., 1997).

4.5 Summary and Outlook

A review of various in situ electrochemical cells for a Li-ion battery investigation is presented. An AFM technique was chosen for this study because it provides high resolution morphological information for samples, it performs well in a liquid environment, and it requires no special sample preparation. It also does not need an

ultra-high vacuum environment to operate. Various electrochemical cell designs using an AFM are described. A wire experimental cell design was chosen because fewer parts were required, thus making assembly in the glove box easier. Lithium wire could also be handled easily without needing any extra preparation. In situ electrochemical AFM studies on the Li-ion battery allow for the accurate measurement of the morphological changes that occur on the cathodes during cycling of the cell at a nanometer scale resolution.

Charge/discharge curves were different for the commercial cell used as a reference than that of the experimental cell. The commercial cell operated as expected from theoretical calculations. The experimental wire cell showed a larger drop in voltage from the end of discharging to the start of charging, and it discharged much faster than the theoretically calculated discharge time. Morphology data, shown in **Fig. 4.7**, shows an increase in particle size from the $FePO_4$ phase to the $LiFePO_4$ phase during the discharge of the cell. This increase in particle size was due to lithiation, and occurred as expected. The particle size reduced from an initial size of 0.30 μm^2 to a size of 0.26 μm^2 when charged, and after discharging the monitored particle size increased from 0.26 μm^2 to 0.33 μm^2.

In situ AFM electrochemical experiments provide useful information about morphological changes during charging and discharging. These experiments can be used for further Li-ion battery characterization. The Li-wire cell design has a large electrolyte area exposed to ambient conditions, which leads to the evaporation of the electrolyte. Hence, a more suitable design may be needed.

Chapter 5: Summary

Increasing awareness of carbon dioxide (CO_2) emissions from traditional gasoline-powered vehicles on the environment has driven research in developing novel energy storage devices for environmentally friendly vehicles. The goal is to reduce the automobile industry's dependence on oil and to ultimately to reduce CO_2 emissions. Advances in Li-ion batteries as an energy storage device have made them a viable option for EVs, HEVs and PHEVs due to their high energy and power density over other battery chemistries. During the operation of a Li-ion battery, charge and discharge cycles reduce its capacity and power. It is therefore important to study the cause of these aging mechanisms in order to increase battery life.

In this thesis work, both ex-situ and in-situ studies were conducted to understand the ageing phenomenon in LiFePO4 cathodes. Higher resolution morphology images and particle size analysis were needed to quantify the coarsening process. Conductivity studies were done to quantify the electrical conductivity difference between unaged and aged cathodes related to agglomerated regions in high resolution image. Nanomechanical and mechanical integrity characterization were conducted to investigate the effect of increased internal stress during aging on nanomechanical and mechanical integrity properties. In situ AFM electrochemical characterization was conducted for direct observation of morphological changes in cathode during cycling.

High resolution images of aged and unaged $LiFePO_4$ cathodes were obtained at different scan sizes; upon analysis of particle size and roughness, it was found that the surface of the aged cathodes showed particle agglomeration. The agglomerated particles are believed to consist of small particles. Conductivity measurements showed the aged samples to have poor electrical conductivity. The carbon coating on the $LiFePO_4$ nanoparticles needed for enhancing electrical conductivity might be degraded during agglomeration and accounts for the observed morphological changes. The loss of contact of the active material from the current collector and the, possible loss of carbon coating led to increased resistance in the cathode and hence significantly lowered conductivity. These degradation issues created morphological and conductivity changes that reduce battery capacity and ultimately led to reduced battery life.

Nanomechanical characterization and mechanical integrity studies were carried out to determine the effect of change in physical and chemical properties and the increase in internal stresses during aging. Measured nanomechanical properties included hardness, elastic modulus, and creep, while mechanical integrity properties of unaged and aged $LiFePO_4$ battery cathodes include nanowear, nanoscratch and nanofriction. The aged cathodes showed higher hardness, creep depth and critical load in scratch and lower wear depth and coefficient of friction. Higher hardness in the aged cathodes is believed to make it brittle, and during scratch test, catastrophic damage was observed. Increase in creep depth is believed to be due to binder degradation during aging.

A review of various in-situ electrochemical cells for Li-ion battery investigation is presented. An AFM technique was chosen for this study because it provides high resolution morphological information for samples, performs well in liquid environments, and requires no special sample preparation. In situ electrochemical cells were designed to allow AFM studies on cathodes to be conducted while cells were being cycled. This provided morphological images of the cathode at nanometer scale resolution. Morphology data showed an increase in particle size from the $FePO_4$ phase to $LiFePO_4$ phase during discharge of the cell due to lithiation; this was expected.

In situ AFM electrochemical experiments provides useful information about morphology changes during charge and discharge and can be used for further Li-ion battery characterization. Electrolyte evaporation from in situ AFM electrochemical cells remains a prominent problem, as this affects the time at which the cell can be cycled. Improved cell design is needed for advancement of this field.

References

Anonymous, (2002), FreedomCAR 42 V Energy Storage System End-of-Life Performance Goals, Southfield, MI, USABC.
Available from: <http://www.uscar.org/guest/view_team.php?teams_id=12>.

Anonymous, (2006a), USABC Goals for Advanced Batteries for EVs, Southfield, MI, USABC. Available from: <http://www.uscar.org/guest/view_team.php?teams_id=12>

Anonymous, (200b), USABC Requirements of End of Life Energy Storage Systems for PHEVs, Southfield, MI, USABC.
Available from: <http://www.uscar.org/guest/view_team.php?teams_id=12>

Armand, M. and Tarascon, J. M., (2008), "Building better batteries," *Nature*, **451**, 652-657.

Balke, N., Jesse, S., Morozovska, A.N., Eloseev, E., Kim, Y., Adamczyk, L., Garcia, R.E., Dudney, N., and Kalinin, S.V. (2010), "Nanoscale mapping of ion diffusion in a lithium - ion battery cathode," *Nat. Nanotechnol* **5**, 749-754.

Bhushan, B. (2011), *Nanotribology and Nanomechanics Vol. I and II, 3rd ed.*, Springer, Heidelberg, Germany.

Bhushan, B. (2013), *Introduction to Tribology*, Second ed., Wiley, New York.

Borong, W., Ren, Y. and Li, L. (2011), "LiFePO4 Cathode Material," in: *Electric Vehicles - The Benefits and Barriers*, (Edited by Soylu, S.), pp. 199-202, InTech, Europe.

Brazier, A., Dupont, L., Dantras-Laffont, L., Kuwata, N., Kawamura, J. and Tarascon, J. M. (2008), "First cross-section observation of an all solid-state Li-ion "nanobattery" by Transmission Electron Microscopy," *Chem. Mater.* ***20***, 2352–2359.

Campana, F. P., Kotz, R., Vetter, J., Novak, P., Siegenthaler, H. (2005), "In-situ atomic force microscopy study of dimensional changes during Li^+ ion intercalation/de-intercalation in highly oriented pyrolitic graphite," Electrochem. Commun. 7, 107-112.

Chao, S. C., Yen, Y. C., Song, Y. F., Sheu, H. S., Wu, H. C. and Wu, N. L. (2011), “In situ transmission x-ray microscopy study on working SnO anode particle of Li-ion batteries,” *J. Elec. Soc*. 158, A1335-A1339.

Chen, J., Bull, S. J., Roy, S., Kapoor, A., Mukaibo, H., Nara, H. and Momma, T. (2009), "Nanoindentation and nanowear study of Sn and Ni-Sn coatings," *Trib. Inter.* ***42***, 779-791.

Chen, D., Indris, S., Schulzc, M., Gamera, B. and Mönига, R. (2011), "In situ scanning electron microscopy on lithium-ion battery electrodes using an ionic liquid," *J. Power Sources,* ***196***, 6382–6387.

Chen, G., Song, X. and Richardson, T.J. (2006), "Electron Microscopy Study of the $LiFePO_4$ to $FePO_4$ Phase Transition," *J. Electrochem. Soc.***9**, A295–A298.

Choi, D., Wang, W. and Yang, Z. (2012), “Material challenge and perspective," in: Lithium-ion Batteries: Advanced Materials and Technologies (Edited by Yuan, X., Liu, L. and Zhan, J.), pp. 1-16, CRC Press, New York, USA.

Chung, S.Y., Bloking, J.T. and Chiang, Y.M. (2002), “Electronically conductive phospho-olivines as lithium storage electrodes,” *Nature Mater.* **2**, 123–128.

Christensen, J. and Newman, J. (2006), "Stress generation and fracture in lithium insertion material," *J. Solid. St. Electrochem*. **10**, 293-319.

Deb, A., Bergmann, U., Cairns, E, J., Cramer, S. P., (2004), “X-ray absorption spectroscopy study of Li_xFePO_4 cathode during cycling using a novel electrochemical in situ reaction cell,” *J. Synchrotron Rad,* **11**, 487-504.

Deb, A., Bergmann, U., Cramer, S. P., Cairns, E, J., (2007), “In situ X-ray absorption spectroscopy study of $LiNi_{1.05}Ni_{0.35}Co_{0.25}Mn_{0.4}O_2$ cathode material coated with $LiCoO_2$,” *J. Electrochem. Soc.*, ***154***, A534-A541.

Doi, T., Inaba, M., Tsuchiya, H., Jeong, S. K., Iriyama, Y., Abe, T. and Ogumi, Z. (2008), "Electrochemical AFM study of $LiMn_2O_4$ thin film electrodes exposed to elevated temperatures," *J. Power Sources,***180**, 539-545.

Elazari, R., Salitra, G., Toyosef, Y., Grinblat, J., Scordilis-Kelly, C., Xiao, A., Affinito, J. and Aubach, D. (2010), "Morphological and structural studies of composite sulfur electrodes upon cycling by HRTEM, AFM and Raman Spectroscopy,*" J. Electrochem. Soc.***157**, A1131–A1138.

Fisher, C.A.J. and Islam, M.S. (2008), "Surface structures and crystal morphologies of $LiFePO_4$: relevance to electrochemical behavior," *J. Mater. Chem.*, **12**, 1209-1215.

Goodenough, J. B. (2007), "Cathode materials: A personal perspective," *J. Power Sources* **174**, 996-1000.

Hackney, S. A., Aifantis, K. E., Tangtrakarn, A. and Shrivastava, S. (2012), "Using the Kelvin-Voit model for nanoindentation creep in Sn-C/PVDF nanocomposites," *Mater. Sci. Technol.* **28**, 1161-1165.

Harris, S. J., Timmons, A., Baker, D. R., Monroe, C. (2010), "Direct in situ measurement of Li transport in Li-ion battery negative electrode," *Chemical Physics Letters*, 485, 265-274.

Huang, H. Y. S. and Wang, Y. R. (2012), "Dislocation based stress development in lithium-ion batteries," *J. Electrochem. Soc*. **159**, A815-A821.

Inaba, M., Jeong, S. K. and Ogumi, Z., (2005), "In situ scanning probe microscopy of interfacial phenomena in batteris," *Electrochem. Soc. Inter. Fall*, 55-59.

Kerlau, M., Marcinek, M., Srinivasan, V. and Kostecki, R. (2007), "Studies of local degradation phenomena in composite cathodes for lithium-ion batteries," *Electrochim. Acta* **52,** 5422-5429.

Kostecki, R. and McLarnon, F. (2002), "Degradation of $LiNi_{0.8}Co_{0.2}O_2$ cathode surfaces in high-power lithium-ion batteries," *Electrochem. Solid State Letters* **5**, A164-A166.

Lei, K. L., McLarnon. F. and Kostecki, R. (2005), "In situ raman microscopy of individual $LiNi_{0.8}Co_{0.15}Al_{0.05}O_2$ particles in Li-ion battery composite cathode," *J. Phys. Chem. B.* **109**, 952-957.

Liu, X. H. and Huang, J.Y. (2011), "In situ TEM electrochmistry of anode materias in lithium ion batteries," *Energy Environ. Sci.,* **4**, 3844-3860.

Liu, X. H., Liu, Y., Kushuma, A., Zhang, S., Zhu, T., Li, J. and Huang, Y. (2012), "In situ TEM experiments of electrochemical lithiation and delithiation of individual nanostructures," *Adv. Energy Mater.,* **2**, 722-741.

Meethong, N., Huang, H. Y. S., Speakman, S. A. Carter, W. C. and Chaing, Y. M. (2007), "Strain accommodation during phase transformations in olivine-based cathodes as a materials selection criterion for high-power rechargeable batteries," *Adv. Func. Mat.* **17**, 1115-1123.

Meng, Y. S., McGilvray, T., Yang, M. C., Cotovic, D., Wang, F., Xeng, D., Zhu, Y. and Greatz, J. (2011), " In situ analytical electron microscopy for probing nanoscale electrochemistry," *Electrochem. Soc. Interf. Fall,* 49-52.

Nagpure, S. C. (2011). *Multi-scaled characterization of aged li-ion battery materials for improving performance,* Ph.D. Thesis, The Ohio State University, Department of Mechanical and Aerospace Engineering , Columbus, Ohio.

Nagpure, S. C. and Bhushan, B. (2009), "Atomic force microscopy studies of aging mechanisms in lithium -ion batteries,*" in Applied Scanning Probe Microscopy Methods-Biomimetics and Industrial Applications* (Edited by Bhushan, B. and Fuchs, H.), vol. 13, pp. 203-233, Springer, Heidelberg, Germany.

Nagpure, S. C., Bhushan, B. and Babu, S. S. (2011), "Surface potential measurement of aged li-ion batteries using kelvin probe microscopy," *J. Power Sources* **196**, 1508-1512.

Nagpure, S. C., Bhushan, B. and Babu, S. (2013), "Multi-scaled characterization studies of aged Li-ion large format cells for improving performance - an overview," (unpublished).

Nagpure, S. C., Bhushan, B., Babu, S. and Rizzoni, G. (2009), "Scanning spreading resistance characterization of aged li-ion batteries using atomic force microscopy," *Script.Mater.* **60**, 933-936.

Nagpure, S. C., Dinwiddie, R., Babu, S. S., Rizzoni, G., Bhushan, B. and Frech, T. (2010), "Thermal diffusivity study of aged li-ion batteries using flash method," *J. Power Sources* **195**, 872-876.

Nagpure, S. C., Downing, R. G., Bhushan, B., Babu, S. and Cao, L. (2011), "Neutron depth profiling technique for studying aging in Li-ion batteries," *Electrochim. Acta **56***, 4735-4743.

Neudecker, B. J., Dudney, N. J. and Bates, J. B. (2000), "Lithium-free thin-film battery with in situ plated Li anode," *J. Electrochem. Soc.*, **147**, 517-523.

Oliver, W. C. and Pharr, G. M. (1992) “An improved technique for determining hardness and elastic modulus using load and displacement sensing indentation experiments,” *J. Mat. Res.* **7**, 1564-1583.

Orsini, F., Du Pasquier, A., Beaudoin, B., Tarascon, J. M., Trentin, M., Langenhuizen, N., De Beer, E. and Notten, P. (1998), “In situ scanning electron microscopy (SEM) observation of interfaces withing plastic lithium batteries,” *J. Power Sources,* **76**, 19-29.

Oudenhoven, J. F. M., Labohm, F., Mulder, M., Niessen, R. A. H., Mulder, F. M. and Notten, P. H. L. (2011), "In Situ Neutron Depth Profiling: A Powerful Method to Probe Lithium Transport in Micro-Batteries," *Adv. Mater.* **11**, 1–4.

Padhi, A.K., Najundaswamy, K.S. and Goodenough, J.B. (1997), “Phospho-olivines as Positive-Electrode Materials for Rechargeable Lithium Batteries,” *J. Electrochem. Soc*. **144**, 1188–1194.

Panitz, J. C., Novak, P. and Haas, O. (2001), "Raman microscopy applied to rechargeable lithium -ion cells-steps towards in situ Raman imaging with increased optical efficiency," *App. Spec.*, **55**, 1131-1137.

Park, J., Kalnaus, S., Han, S., Lee, Y. K., Less, G. B., Dudney, N. J., Daniel, C. and Sastry, A. M. (2013), " In situ atomic force microscope studies on lithium (de)intercalation-induced morphology changes in Li_xCoO_2 micro-machined thin film electrodes," *J. Power Source,* **222**, 417-425.

Park, M., Zang. X., Chung. M., Less. G.B., Sastry.A.M. (2010), "A review of conduction phenomena in Li-ion batteries," *J.Power Sources* **195**, 7904-7929.

Raimann, P. R., Hochgatterer, N. S., Korepp, C., Möller, K. C., Winter, M., Schröttner, H., Hofer, F. and Besenhard, J. O. (2006), "Monitoring dynamics of electrode reactions in Li-ion batteries by in situ ESEM," *Ionics,* **12,** 253–255.

Ramdon, S. and Bhushan, B. (2012), "High resolution morphology and electrical characterization of aged Li-ion battery cathode," *J. Colloid Interf. Sci*. **380**, 187-191.

Ramdon, S. and Bhushan, B. (2013), “Nanomechanical characterization and Mechanical integrity of unaged and aged Li-ion battery cathodes," *J. Power Sources,* **246**, 219-222.

Ramdon, S., Bhushan, B. and Nagpure, S. C. (2013), “In-situ AFM electrochemical characterization of Li-ion battery cathodes,” (submitted).

Roberts, M., Biendicho, J. J., Hull, S., Beran, P., Gustafsson, G. S. and Edstrom, K. (2013), “Design of a new lithium ion battery test cell for in-situ neutron diffraction measurements,” *J. Power Sources,* **226**, 249-255.

Shim, J., Kostecki, R., Richardson, T., Song, X. and Striebel, K.A. (2002), "Electrochemical analysis for cycle performance and capacity fading of a lithium-ion battery cycled at elevated temperature," *J. Power Sources* **112**, 222-230.

Srinivan, V. and Newman, J. (2004), "Discharge model for the Lithium Iron- Phosphate electrode," *J. Electrochem. Soc*. **151**, A1517-A1529.

Tarascon, J. M. and Armand M. (2001), “Issues and challenges facing rechargeable lithium batteries,” *Nature*, **414**, 357-367.

Thomas, T.R. (1999), *Rough surfaces*, Second edition, Imperial College Press, London, UK.

Unocic, R. R., Baggetto, L., Unocic, K. A., Veith, G. M., Dudnet, N. J. and More, K. L. (2012), " Coupling EELS/EFTEM imaging with Environmental fluid cell microscopy," *Mocrosc. Microanal.* **18**, 1104-1105.

Vidu, R., Quinlan, F. T. and Stroeve, P. (2002), " Use of in situ electrochemical AFM to monitor cathode surface reachetion in organic electrolyre," *Ind. Eng. Chem. Res.* **41**, 6546-6554.

Wang, H., Downing, R. G., Dura, J. A. and Hussey, D. S. (2012), " In situ neutron techniques for studying lithium ion batteries," in: *Polymers for energy storage and delivery: polyelectrolytes for batteries and fuel cells* (Page, K et al.), pp. 91-106, ACS symposium series, American Chemical Society, Washington, DC, USA.

Yang, Z., Zhang, J., Kintner-Meyer, M.C., Lu, X., Choi, D., Lemmon, J.P. and Liu, J. (2011), "Electrochemical energy storage for green grid," Chem. Rev.111, 3577–3613.

Zaghib, K., Mauger, A., Godenough, J. B. and Julien, C. M. (2013), "Design and Properties of $LiFePO_4$ Nano-materials for High-Power Applications," in: *Nanotechnology for Lithium-Ion Batteries* (Edited by Abu-Lebdeh, Y. and Davidson, I.), pp. 179-182, Springer, Heidelberg, Germany.

Zang, X., Kostecki, R. and McLarnon, F. (2001), "Diagnostic characterization of high power lithium-ion batteries for use in hybrid electric vehicles," *J. Electrochem. Soc.* **148**, A463-A470.

Zhang, X., Shyy, W., Sastry, A. M. (2007), "Numerical simulation of intercalation-induced stress in li-ion battery electrode particles," *J. Electrochem. Soc*. **154**, A910-A916.

Wang, D., Wu, X., Wang, Z. and Chen, L. (2005), "Cracking causing cyclic instability of $LiFePO_4$ cathode material," *J. Power Sources* **140**, 125-128.